RESEARCH ARTICLE

Characterizing digital microstructures by the Minkowski-based quadratic normal tensor

Felix Ernesti[1] | **Matti Schneider**[1] | **Steffen Winter**[2] | **Daniel Hug**[2] | **Günter Last**[2] | **Thomas Böhlke**[1]

[1]Institute of Engineering Mechanics, Karlsruhe Institute of Technology (KIT), Karlsruhe, Germany

[2]Institute of Stochastics, Karlsruhe Institute of Technology (KIT), Karlsruhe, Germany

Correspondence
Matti Schneider, Karlsruhe Institute of Technology (KIT), Institute of Engineering Mechanics, Germany.
Email: matti.schneider@kit.edu

Communicated by: K. Gürlebeck

For material modeling of microstructured media, an accurate characterization of the underlying microstructure is indispensable. Mathematically speaking, the overall goal of microstructure characterization is to find simple functionals which describe the geometric shape as well as the composition of the microstructures under consideration and enable distinguishing microstructures with distinct effective material behavior. For this purpose, we propose using Minkowski tensors, in general, and the quadratic normal tensor, in particular, and introduce a computational algorithm applicable to voxel-based microstructure representations. Rooted in the mathematical field of integral geometry, Minkowski tensors associate a tensor to rather general geometric shapes, which make them suitable for a wide range of microstructured material classes. Furthermore, they satisfy additivity and continuity properties, which makes them suitable and robust for large-scale applications. We present a modular algorithm for computing the quadratic normal tensor of digital microstructures. We demonstrate multigrid convergence for selected numerical examples and apply our approach to a variety of microstructures. Strikingly, the presented algorithm remains unaffected by inaccurate computation of the interface area. The quadratic normal tensor may be used for engineering purposes, such as mean field homogenization or as target value for generating synthetic microstructures.

KEYWORDS
digital image-based, microstructure characterization, Minkowski tensor, quadratic normal tensor

MSC CLASSIFICATION
62

1 | INTRODUCTION

1.1 | State of the art

The effective mechanical and thermal behavior of heterogeneous materials is strongly affected by their microstructure and the local material properties. In particular, macroscopic material models need to account for the microstructure of these materials. Since resolving the microstructure for simulations on component scale is computationally expensive,

homogenization-based multiscale approaches are popular; see Matouš et al[1] for a recent overview. These homogenization techniques compute the effective response of the heterogeneous material, taking the material behavior of the constituents and the microstructure into account. Therefore, the microstructure has to be quantified in terms of suitable data, which is where microstructure characterization comes into play.

A common image-based microstructure characterization method is scanning a material sample via microcomputed tomography (μ-CT).[2,3] After tomographic reconstruction, the local mass density of a material is determined and stored as 3D voxel data. In case of a two-phase material and after some processing, this voxel data may be interpreted as the characteristic function of the microstructure, that is, the function which attains the value 1 for one phase, and the value 0 for the complementary phase. Correctly segmenting μ-CT scans requires a certain contrast in the absorption rates of the constituents to be applicable, for instance, for porous media or for a variety of composite materials.

The mechanical behavior of composite and porous materials is strongly influenced by the volume fractions of the phases. If the characteristic function is accurately resolved by the μCT scan, the volume fraction can be computed accurately by numerical integration. With the volume fraction at hand, bounds that predict the possible range of effective elastic and thermal material properties may be established; see Voigt[4] and Reuss.[5] However, for a high material contrast, these bounds span a wide range and hence provide limited information.

For higher accuracy, additional information is required; see Torquato[6] for an overview. For instance, n-point correlation functions[7,8] provide suitable additional information. Their applicability for anisotropic materials, however, is limited due to the high associated computational effort; see Eriksen et al.[9]

For the class of fiber-reinforced composites, specific microstructure characterization techniques have been established. In addition to the fiber volume fraction, common characteristics include the fiber aspect ratio and fiber orientation tensors of second and fourth orders[10,11]; see, for instance, Müller and Böhlke.[12] A variety of methods for computing fiber orientation tensors based on volumetric images have been established.[13,14] A common approach is based on the so-called structure tensor.[15]

For porous structures, different microstructure characteristics are of interest. For instance, the tortuosity[16] and chord-length distribution,[6,17] as well as the pore-size distribution[18] are investigated. These measures are primarily responsible for the effective (isotropic) permeability of the porous medium in question.

Polycrystalline materials require a different approach. Typically, the grains differ only in their crystalline orientation but have identical absorption rates. Hence, μ-CT scans are of limited use. Instead, for reconstructing the 3D-microstructure of polycrystalline materials, focused ion beam-scanning electron microscopy (FIB-SEM)[19–21] or electron back-scattering diffraction (EBSD)[22–24] is preferred. Primary microstructure characteristics of polycrystalline materials are the grain size distribution (morphological texture)[25] and the orientation distribution (crystallographic texture).[26–30]

From a theoretical point of view, most materials undergoing a manufacturing process are influenced by stochastic factors, for instance, due to slight variations in the composition or the seemingly chaotic behavior of the processing condition as a result of a high sensitivity to initial and boundary conditions. Still, the experimentally determined effective properties of such composites are often surprisingly deterministic. These observations may be formalized by the theory of stochastic homogenization.[31,32] From this stochastic point of view, any finite volume element represents only a fraction of a specific realization of a random material.[6,33] In particular, any quantity associated to such a volume element may also be considered as a *random variable*. For this work, we assume the volume element to be given and fixed and regard the associated quantities as *deterministic*.

Minkowski functionals,[34,35] also known as intrinsic volumes, are a basic tool in stochastic geometry. They are defined for wide classes of shapes, including all convex sets and their finite unions as well as all bounded sets with smooth boundary. A Minkowski functional associates to any such shape a scalar quantity. If one requires such a functional to be invariant with respect to Euclidean motions, additive, and to satisfy a certain continuity property, then it can be shown, see Hadwiger,[35] that in 3D it can be written as linear combination of only four *basic* functionals, the Minkowski functionals. Among them are the total volume, the total surface area, the Euler characteristic and one further functional, which for convex shapes may be interpreted as the mean width or in the context of smooth boundaries as the integral of mean curvature. Approaches for computing Minkowski functionals are based, for instance, on marching squares[36] or on Steiner's formula.[37,38]

Being scalar-valued and rotation invariant, Minkowski functionals are intrinsically insensitive to anisotropic features of the shape in question. Therefore, tensor-valued analogs of Minkowski functionals, the so-called Minkowski tensors,[39–42] were introduced and studied. In addition to additivity and continuity, Minkowski tensors are required to be equivariant w.r.t. Euclidean transformations. This means, for instance, that rotating a shape first and computing its Minkowski tensor afterwards leads to the same result as computing the Minkowski tensor first and rotating the tensor afterwards. A direct

consequence of this property is that Minkowski tensors preserve axes of symmetry of structures, that is, if a shape is rotationally invariant w.r.t. an axis $\mathbf{p}$, the Minkowski tensor will be rotationally invariant w.r.t. $\mathbf{p}$ as well.

Minkowski tensors may be computed for general microstructures with distinct interfaces, such as porous media, foams, bones, or granular structures.[43] For porous media, Klatt et al[44] conducted a comparison between the common chord-length analysis and a Minkowski tensor-based approach. Schroeder-Turk et al[43,45] evaluated Minkowski tensors for a given triangulation of the interface via explicitly known expressions for polytopes. Their ansatz was successfully used for characterizing the anisotropy of granular matter and metal foams, as well as identifying defects in molecular dynamics simulations of metal phases. For 3D gray value images, Svane[46,47] introduced approximation formulae for Minkowski functionals and tensors, also establishing convergence upon mesh refinement, called multigrid convergence in this context. Unfortunately, the cited works[46,47] did not include numerical examples.

For finite point samples, Voronoi-based estimators[48] may be used for approximating Minkowski tensors.

1.2 | Contributions

We present an applied approach for characterizing digital microstructures of industrial complexity in terms of the quadratic normal tensor (QNT), a tensor-valued quantity based on Minkowski tensors, bringing these concepts to the attention of the engineering community.

For phenomenological continuum theories, which use microstructure information as state or microstructure variables to model the influence of microstructure on macroscopic material behavior, the Minkowski tensors are promising quantities, because they are in principle observable and can be effectively calculated from three-dimensional image data. The Minkowski tensors complement, for example, the already widely used fiber orientation tensors,[10,11] which approximate the tangent distribution of the fiber centerline, and tensorial texture coefficients,[27,30] which describe the distribution of crystal orientations.

We introduce the relevant Minkowski functionals and tensors in Section 2 and isolate among them those suitable for microstructure characterization. In Section 3, we present a novel algorithm for computing the QNT. For large microstructures with complex geometry, finding triangulations of the interface may be a challenging task, in particular, if the microstructure is described by voxel data. Therefore, we present here an alternative to triangulation-based algorithms[43] that work directly with gray value images as input. The outward-pointing unit normals on the materials interface are approximated by finite- difference gradients of the discretized characteristic function.

We investigate multigrid convergence of our approach by numerical studies in Section 4. For fiber-reinforced composites, we compare the QNT to the more conventional fiber orientation tensor of second order.[10,11] We compare the accuracy of our approach to the commonly used structure tensor-based algorithm[15] for computing fiber orientation tensors. Last but not least, we study the anisotropy of sand grains and porous sand binder aggregates based on the QNT.

2 | USING MINKOWSKI TENSORS FOR DESCRIBING MICROSTRUCTURES

2.1 | Minkowski tensors

We briefly introduce Minkowski functionals and Minkowski tensors in a form suitable for our purposes and restrict to the 3D case. We refer to Schröder-Turk et al[43,45] or the lecture notes[42] for the general case.

Consider a solid body, by which we mean a bounded, not necessarily connected set K in $\mathbb{R}^3$ with sufficiently regular boundary ∂K. Here regularity can mean smoothness or convexity of some form. For our purposes, it will be completely sufficient to assume that K is polyconvex, that is, K can be represented as a finite union of (not necessarily disjoint) convex sets.

To gain insight into the morphology of K, a shape index φ associates to any such set K a scalar value. If one requires the shape index φ to satisfy some natural basic properties, namely, invariance with respect to rigid motions, additivity (meaning that $\varphi(K \cup L) = \varphi(K) + \varphi(L) - \varphi(K \cap L)$ for solid bodies (K, L), and a certain continuity (for convex sets, and w.r.t. the Hausdorff distance, see, e.g., Schneider-Weil[34, §12.3]), then it is a well-known fact due to Hadwiger,[35] that φ may be represented as a linear combination of only four basic functionals $V_0, \ldots, V_3$, known as Minkowski functionals or intrinsic volumes. The Minkowski functionals encompass the volume $V = V_3$, the surface area $S = 2V_2$, and two further functionals, V_1 and V_0, which in special situations can be interpreted as the total mean curvature and the total Gaussian curvature of the body K. The latter is proportional to the Euler characteristic of K, that is, the genus of the surface ∂K, which is a topological invariant. Volume and surface area are computed by
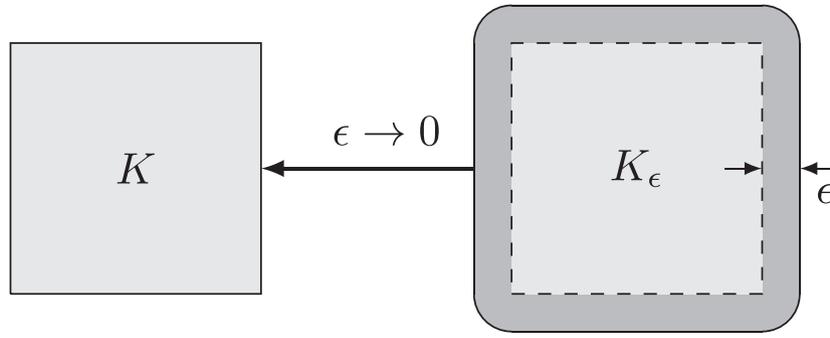
FIGURE 1 Illustration of the ε-parallel expansion K_ε of the shape $K \subseteq \mathbb{R}^3$

$$V(K) = \int_K dV \quad \text{and} \quad S(K) = \int_{\partial K} dS. \tag{2.1}$$

If the boundary ∂K is sufficiently smooth, then the local mean curvature H and the Gaussian curvature G (i.e. the average and the product of the principal curvatures) are well-defined at each boundary point and the total curvatures may be computed via

$$V_1(K) = \frac{1}{\pi} \int_{\partial K} H \, dS \quad \text{and} \quad V_0(K) = \frac{1}{4\pi} \int_{\partial K} G \, dS. \tag{2.2}$$

Such integral representations are also available for non-smooth bodies when one replaces ∂K by an integration over the normal bundle of K.[49] For practical computations, the additivity property is essential, allowing to decompose complex structures into simple convex pieces and to treat these pieces individually. For convex shapes, the Steiner formula provides another way to characterize the Minkowski functionals and another idea how to compute them. Consider, for a convex body K and $\varepsilon > 0$, the ε-approximation

$$K_\varepsilon = \left\{ \mathbf{x} \in \mathbb{R}^3 : ||\mathbf{x} - \mathbf{y}|| \leq \varepsilon \text{ for some } \mathbf{y} \in K \right\};$$

see Figure 1 for a schematic illustration. The Steiner formula[50] states that the volume of K_ε is a polynomial in ε, whose coefficients are (up to some normalization constants) the Minkowski functionals of K:

$$V(K_\varepsilon) = V(K) + \varepsilon S(K) + \pi \varepsilon^2 V_1(K) + \frac{4\pi}{3} \varepsilon^3 V_0(K). \tag{2.3}$$

This allows to recover the Minkowski functionals of K by computing volumes of a number of ε-approximations and inverting the above formula; see Klenk-Schmidt-Spodarev.[51] One can also use the fact that the ε-approximations K_ε are smooth even if K is not, allowing to determine the Minkowski functionals V_1 and V_0 by means of the limit procedure

$$V_1(K) = \lim_{\varepsilon \to 0} V_1(K_\varepsilon) \quad \text{and} \quad V_0(K) = \lim_{\varepsilon \to 0} V_0(K_\varepsilon).$$

While these approximation results follow from the continuity of the Minkowski functionals, ε-approximation properties of more general classes of sets are discussed in Rataj.[52] For more background to our informal discussion, we refer to Schröder-Turk et al[45] and the references therein.

Since Minkowski functionals are, by definition, invariant w.r.t. Euclidean motions or change of frame, they are insensitive to directional and positional information. Hence, they are inappropriate for detecting anisotropies in a shape K. For this latter purpose and other applications, a more general theory of tensor-valued shape indices has been developed, which are covariant w.r.t. Euclidean motions; see Schröder-Turk et al.[45] In analogy to Hadwiger's theorem[35] and restricting to $\mathbb{R}^3 \otimes_{\text{sym}} \mathbb{R}^3 \cong \mathbb{R}^{3 \times 3}_{\text{sym}}$ tensors, there are only six linearly independent shape indices (in addition to the Minkowski functionals multiplied by the identity); see Alesker et al[39] and in particular earier studies.[40, §4] For a (convex) body K with

sufficiently smooth boundary, these may be expressed as follows:

$$W_0^{2,0}(K) = \int_K \mathbf{x} \otimes \mathbf{x} \, dV, \qquad W_1^{2,0}(K) = \frac{1}{3}\int_{\partial K} \mathbf{x} \otimes \mathbf{x} \, dS, \quad W_2^{2,0}(K) = \frac{1}{3}\int_{\partial K} H(\mathbf{x})\mathbf{x} \otimes \mathbf{x} \, dS,$$

$$W_3^{2,0}(K) = \frac{1}{3}\int_{\partial K} G(\mathbf{x})\mathbf{x} \otimes \mathbf{x} \, dS, \quad W_1^{0,2}(K) = \frac{1}{3}\int_{\partial K} \mathbf{n} \otimes \mathbf{n} \, dS, \quad W_2^{0,2}(K) = \frac{1}{3}\int_{\partial K} H(\mathbf{x})\mathbf{n} \otimes \mathbf{n} \, dS. \tag{2.4}$$

Here, $\mathbf{x}$ denotes the position vector of a point in K (or ∂K) and $\mathbf{n}$ stands for the field of outward-pointing unit normal vectors on ∂K. For Minkowski tensors, Steiner-type formulae based on support measures have been established; see Schneider.[53] Note that some Minkowski functionals can be recovered from Minkowski tensors. For instance, the surface area is given by the formula $S(K) = 3\mathrm{tr}(W_1^{0,2}(K))$.

Based on these Minkowski tensors, Schröder-Turk et. al.[43] introduce the eigenvalue ratios

$$\beta(W) = \frac{\min\limits_{\lambda \in \mathrm{E}(W)} |\lambda|}{\max\limits_{\lambda \in \mathrm{E}(W)} |\lambda|}, \tag{2.5}$$

as scalar measures of anisotropy. Here W stands for any of the six Minkowski tensors defined in (2.4) and $\mathrm{E}(W)$ is the set of eigenvalues of the symmetric matrix W. Clearly, $\beta(W) \in [0, 1]$. For $W = W_0^{2,0}$, $W_1^{2,0}$, and $W_1^{0,2}$, the matrix $W(K)$ is positive semidefinite in general (and this is also true for the other Minkowski tensors if K is a convex body), implying that all eigenvalues of W are nonnegative. In this case, $\beta(W) = 1$ if and only if all eigenvalues are equal, that is, if the tensor is a multiple of the identity. Note that smaller values of $\beta(W)$ correspond to a higher degree of anisotropy.

2.2 | Minkowski tensor-based microstructure characterization

Heterogeneous materials often exhibit random variations in their microstructure but a resulting deterministic material behavior.[6] For characterizing microstructures, we are interested in singling out a small number of tensor-valued descriptors, that may, in turn, be used as input for homogenization schemes; see Klusemann and Svendsen[54] for an overview. These microstructure identifiers should preferably exhibit certain natural properties:

1. Respect for symmetries: We seek microstructure identifiers that preserve symmetry information. If a microstructure possesses some symmetry, then this is typically reflected in the macroscopic material behavior. Therefore, identifiers should capture such symmetry.
2. Robustness: To be of practical use, small changes in the microstructure should only result in small changes in the descriptor.
3. Translation invariance: For homogenization, statistical homogeneity is essential.[6] Thus, our identifiers should be invariant with respect to translations of the shape K. Furthermore, we want to explicitly include periodic structures, as periodic homogenization is often used for studying random microstructures.[33]
4. Universal applicability: Minimal assumptions on the geometry of the structure allow for general application on a variety of different microstructures.

In the light of these criteria, Minkowski tensors are promising candidates for microstructure characteristics.

1. Their covariant tensorial nature reflects the anisotropy and direction dependence of the structure in question.
2. They are robust due to their continuity properties w.r.t. the Hausdorff distance. For example, if a sequence of convex bodies K_n converges to a convex body K, as $n \to \infty$, then all their Minkowski functionals and Minkowski tensors converge as well. Similar results hold, for example, if a polyconvex set K is approximated by its parallel sets K_ε; see.[50,52] There are also stability results showing Hölder continuity with exponent at least $1/2$.[55]
3. If translation invariance is required, then beside the Minkowski functionals among the above mentioned Minkowski tensors precisely $W_1^{0,2}$ and $W_2^{0,2}$ are suitable. As computing the curvature of interfaces of 3D voxel images is not straightforward,[56,57] we restrict in this article to the volume V, the surface area S, and the Minkowski tensor $W_1^{0,2}$.
4. The Minkowski tensors are not restricted to specific shape assumptions on K. Indeed, only minimal assumptions on K are required.[43] For any practical application, it is probably sufficient to note that any set (however complex) can be approximated arbitrarily well by a polyconvex set on which Minkowski tensors are defined. The tensor $W_1^{0,2}$ under consideration can in fact be defined under much weaker regularity assumptions, for example, for sets with piecewise smooth boundaries. This flexibility distinguishes them from other approaches, where geometric priors are
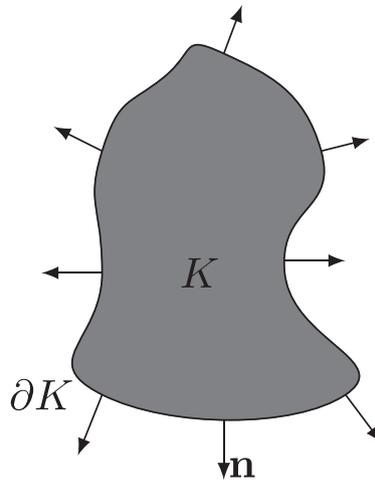
FIGURE 2 Body K with outward-pointing unit normal field $\mathbf{n}$

required for characterizing microstructures. For instance, for fiber-reinforced composites, fibers are often assumed to be (locally) cylindrical. Such geometrical priors run into problems for fibrous microstructure where the fibers deviate from their original cylindrical shape. For instance, during injection molding, fibers may be bent or twisted.[58] As they are independent of priors, Minkowski tensors may be suitable for characterizing fibers with distinct curvature.

In the field of microstructure characterization, K is often the set union of a multitude of bodies, for instance, inclusions within a surrounding matrix material. In this context, we are interested in a tensorial anisotropy-measure, which is stable w.r.t. an infinite-volume limit, where the number of inclusions tends to infinity. Thus, we normalize $W_1^{0,2}$ to obtain the QNT

$$\text{QNT}(K) = W_1^{0,2}(K)/\text{tr}(W_1^{0,2}(K)), \tag{2.6}$$

which, for a single body or microstructure K with sufficiently smooth boundary, may be written in the form

$$\text{QNT}(K) = \frac{1}{S(K)}\int_{\partial K} \mathbf{n} \otimes \mathbf{n}\, dS,$$

where again $\mathbf{n} = \mathbf{n}(\mathbf{x})$ is the field of normal vectors on ∂K; compare Figure 2. For a geometric interpretation of the QNT, observe that for any vector $\xi \in \mathbb{R}^3$, the expression

$$(\mathbf{n} \otimes \mathbf{n})\xi = \mathbf{n}(\mathbf{n} \cdot \xi)$$

describes the orthogonal projection of ξ onto the line spanned by the normal direction $\mathbf{n}$ at $\mathbf{x}$. In this sense, QNT(K) may be interpreted as an average over the normal projections computed w.r.t. the uniform probability measure concentrated on the surface ∂K. (Note that the resulting average matrix is still symmetric and positive definite but does not represent a projection anymore.)

The QNT(K) admits an additional interpretation from a mechanical point of view. Suppose the structure K deforms with a homogeneous stress $\boldsymbol{\sigma}$. Then, contracting the stress tensor with the QNT

$$\text{QNT}(K) : \boldsymbol{\sigma} = \frac{1}{S(K)}\int_{\partial K} \mathbf{n} \cdot (\boldsymbol{\sigma}\mathbf{n})\, dS$$

computes the mean normal stress on the surface ∂K.

By construction, the QNT is symmetric, positive semidefinite, and has trace 1. In particular, QNT(K) admits an eigenvalue decomposition with real-valued, nonnegative eigenvalues λ_1, λ_2, and λ_3, which sum to 1. In case of a convex K, certain eigenvalue combinations can directly be interpreted in terms of the resulting shape of K: $\lambda_1 \gg \lambda_2 = \lambda_3$, for instance, indicates a rather flat shape within the plane perpendicular to the eigenvector corresponding to λ_1. For $\lambda_1 = \lambda_2 \gg \lambda_3$, we expect K to be a needle expanded in the direction of the eigenvector associated with λ_3; see also Appendix A.2, where the QNT is computed for a cylinder, and the sand grain experiments in Section 4.4.

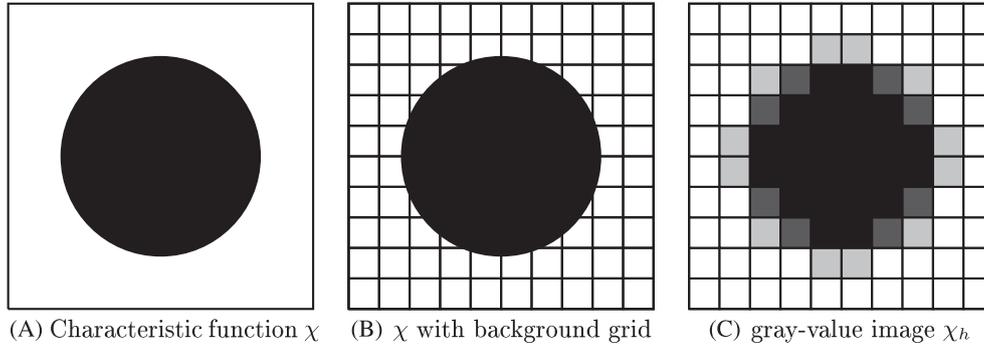(A) Characteristic function χ (B) χ with background grid   (C) gray-value image χ_h

FIGURE 3 Characteristic function of a ball and its discrete representation by a gray value image on a regular voxel grid

Another advantage of Minkowski tensors is that they are locally defined and therefore locally computable. Complex polyconvex shapes can be cut into simple pieces, and each piece can be treated separately. Then the additivity allows to recover the Minkowski tensor of the whole body from the Minkowski tensors of the pieces, allowing for efficient computation and parallelization.

3 | EFFICIENT IMPLEMENTATION FOR 3D IMAGE DATA

3.1 | Algorithmic overview

Consider a (periodic) heterogeneous two-phase material on the domain $Y = [0, L_x] \times [0, L_y] \times [0, L_z]$. The microstructure of the material is described by its characteristic function $\chi : Y \to \{0, 1\}$, defining the two phases Ω_0 and Ω_1 via $\Omega_0 = \{\mathbf{x} \in Y : \chi(\mathbf{x}) = 0\}$ and $\Omega_1 = Y \smallsetminus \Omega_0$, respectively. Our aim is to describe phase Ω_1 using the Minkowski functionals and tensors $V(\Omega_1)$, $S(\Omega_1)$, $W_1^{0,2}(\Omega_1)$, and $\text{QNT}(\Omega_1)$.

Note that Ω_1 is unknown in practice; only CT images of Ω_1 can be observed. μ-CT data are typically stored as 3D gray value voxel data. We interpret the voxel data as a mapping $\chi_h : Y_h \to [0, 1]$ from the discrete set Y_h, comprising the centers of a regular voxel grid with voxel length h, to the unit interval representing gray values. The gray value $\chi_h(\mathbf{y})$ associated to a point $\mathbf{y} \in Y_h$ stands for the volume fraction of Ω_1 in the voxel centered at $\mathbf{y}$. The relation between χ and its discretization χ_h is demonstrated in Figure 3. Figure 3A shows the characteristic function χ of a ball. Figure 3B shows the nondiscretized ball with the regular grid Y_h in the background. In Figure 3C, we see the discrete characteristic function χ_h of this ball as a gray value image.

Note that, in general, the input data χ_h does not allow to recover the phases Ω_0 and Ω_1 exactly as the interface is blurred. Only in the limit as $h \to 0$, the correct characteristic function and, therefore, the correct sets are recovered. For determining $W_1^{0,2}$ and S, in addition, the normal directions are needed. In a weak sense, the unit normal $\mathbf{n}$ of the set Ω_1 at a boundary point is recovered by $\mathbf{n} = -\nabla \chi$, whereas $-\nabla \chi = 0$ away from the boundary. This statement may be formalized in terms of functions of bounded variation.[59] Therefore, we will compute the gradient numerically and establish formulae for $W_1^{0,2}$ and S based on volume averaging; compare Section 3.4. To improve the gradient estimation, a smoothing of the characteristic function χ_h is applied beforehand. The algorithm for computing the Minkowski quantities from a given voxel image is summarized in Algorithm 1. First, we apply an image filter $\mathcal{F}_\sigma$ to the characteristic function χ_h. Secondly, we estimate the outward-pointing normal vector by computing the gradient $\mathbf{g}$ from the resulting smoothed image $\mathcal{I}_h^\sigma$. Finally, the desired quantities V, S, $W_1^{0,2}$, and QNT are estimated.

Algorithm 1 Computation of Minkowski quantities

1: $\mathcal{I}_h^\sigma \leftarrow \mathcal{F}_\sigma * \chi_h$ ▷ Blur image with image filter
2: $\mathbf{g}(\mathbf{x}) \leftarrow \nabla_h \mathcal{I}_h^\sigma(\mathbf{x})$ ▷ Compute gradient
3: Compute V by (3.1)
4: Compute S by (3.2)
5: Compute $W_1^{0,2}$ by (3.3)
6: Compute QNT by $W_1^{0,2}/\text{tr}(W_1^{0,2})$
7: **return** $(V, S, W_1^{0,2}, \text{QNT})$

3.2 | Smoothing by image filters

Due to the reconstruction procedure, μ-CT scans often exhibit artifacts and impurities. Furthermore, binary voxel-based images do not allow reconstructing interfaces accurately.[36] To deal with these issues, we apply an image filter to the discrete characteristic function (prior to computing the gradient). As different filters (and different choices of parameters) are available, we will also address choosing an appropriate filter. Applying the filter is realized by convolving the image with a specific filter kernel $\mathcal{F}_\sigma$. The filter parameter σ controls the width of filtering, and the result is the filtered image $\mathcal{I}_h^\sigma$, given as the convolution

$$\mathcal{I}_h^\sigma = \mathcal{F}_\sigma * \chi_h.$$

In our implementation, the convolution with $\mathcal{F}_\sigma$ is implemented via fast Fourier transform (FFT),[60] see Algorithm 2. Notice that in some cases the Fourier-transformed filter kernel may be computed efficiently without using the FFT.

Algorithm 2 FFT-based filter application

1: $\widehat{\chi_h} \leftarrow \mathrm{FFT}(\chi_h)$ ▷ Transformation of the characteristic function
2: $\widehat{\mathcal{F}_\sigma} \leftarrow \mathrm{FFT}(\mathcal{F}_\sigma)$ ▷ Transformation of the filter kernel
3: $\widehat{\mathcal{I}_h^\sigma}(\xi) \leftarrow \widehat{\chi_h}(\xi)\widehat{\mathcal{F}_\sigma}(\xi)$ ▷ Multiplication in Fourier space for all frequencies ξ
4: $\mathcal{I}_h^\sigma \leftarrow \mathrm{IFFT}(\widehat{\mathcal{I}_h^\sigma})$ ▷ Inverse transformation

---

We shall consider a dimensionless filter parameter σ and scale it by the voxel length h. As filter kernels, we consider a Gaussian kernel[61]

$$\mathcal{G}_\sigma(\mathbf{x}) = \frac{1}{(h\sigma)^3(2\pi)^{\frac{3}{2}}} \exp\left(-\frac{\|\mathbf{x}\|^2}{2(h\sigma)^2}\right)$$

and the characteristic function of the unit ball, scaled to integrate to unity,

$$\mathcal{B}_\sigma(\mathbf{x}) = \begin{cases} \frac{3}{4\pi(h\sigma)^3} & \text{if } \|\mathbf{x}\| \leq h\sigma, \\ 0 & \text{otherwise.} \end{cases}$$

In Figure 4, the effect of filtering by a Gaussian and a ball kernel, respectively, is shown for a 1D laminate structure discretized with a voxel length of $h = 2\,\mu m$ for three different filter parameters σ. The red curve illustrates the impact of the Gaussian filter, whereas the blue line represents the ball-filtered image. In the Gaussian case, the resulting image is smooth across the laminate's interface. However, for larger σ, not only the interface is blurred, but no region of black or white remains. In fact, due to its global support, this even holds for small σ.

The impact of the ball filter is completely different. The piecewise constant indicator function with jumps at the interfaces is transformed into a piecewise linear function with slopes $\pm\frac{1}{2h\sigma}$. Therefore, when applying the ball filter to a structure with diameter larger than $2h\sigma$, some region with $\mathcal{I}_h^\sigma = 1$ will remain.

3.3 | Approximating the surface normal by finite differences

Computing the Minkowski tensor $W_1^{0,2}(\Omega_1)$ requires determining the (unit) normal vector field $\mathbf{n}$ on the surface $\partial\Omega_1$. We approximate the normal field $\mathbf{n}$ by computing the gradient vector field

$$\mathbf{g} = \nabla_h \mathcal{I}_h^\sigma$$

of the filtered image $\mathcal{I}_h^\sigma$ numerically. Notice, that $\mathbf{g}$ is dependent on the voxel length h. At boundary points, we consider $\mathbf{n} \approx -\mathbf{g}/\|\mathbf{g}\|$ as the outward-pointing unit normal, provided $\mathbf{g} \neq 0$. We briefly discuss the choice of the numerical gradient approximation method. Finite difference approximations are a simple way for approximating the gradient of a function given on a regular voxel grid numerically. Suppose a function $f : Y \to \mathbb{R}, \mathbf{x} \mapsto f(\mathbf{x})$ is given. We consider three finite difference discretization schemes for the partial derivative in $\mathbf{e}_i$-direction ($i = 1, 2, 3$):

1. first-order approximation by forward differences, i.e.,

$$\partial_i^h f(\mathbf{x}) \approx \frac{f(\mathbf{x} + h\mathbf{e}_i) - f(\mathbf{x})}{h};$$
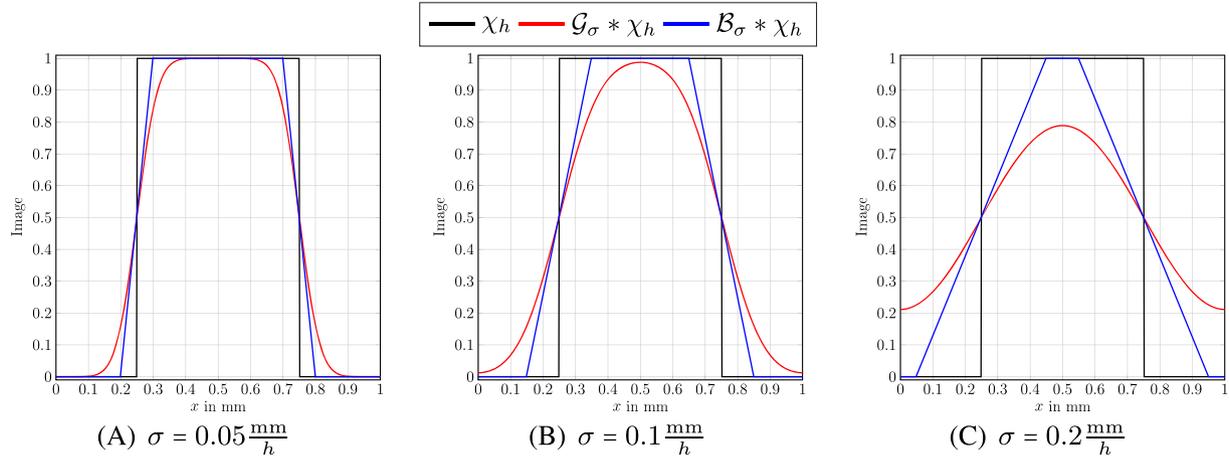
(A) $\sigma = 0.05 \frac{mm}{h}$ (B) $\sigma = 0.1 \frac{mm}{h}$ (C) $\sigma = 0.2 \frac{mm}{h}$

FIGURE 4 Influence of filtering with different kernels and widths σ [Colour figure can be viewed at wileyonlinelibrary.com]

2. first-order approximation by backward differences, i.e.,

$$\partial_i^h f(\mathbf{x}) \approx \frac{f(\mathbf{x}) - f(\mathbf{x} - h\mathbf{e}_i)}{h};$$

3. second-order approximation by central differences, i.e.,

$$\partial_i^h f(\mathbf{x}) \approx \frac{f(\mathbf{x} + h\mathbf{e}_i) - f(\mathbf{x} - h\mathbf{e}_i)}{2h}.$$

Since our numerical experiments are performed on periodic structures, we treat the boundary in a periodic fashion. Under certain regularity assumptions on the function to differentiate, the first-order approximations converge linearly in h to the exact gradient, whereas the second-order approximation converges quadratically as $h \to 0$; see Olver.[62] However, some further differences arise, which we demonstrate by example; see Figure 5.

Consider the filtered gray value image of a ball, shown in Figure 5A. When computing the gradient via central differences, the symmetry of the structure is recovered in the symmetry of the gradient field, since $\mathcal{I}_h^\sigma(\mathbf{x})$ and $\mathbf{n}(\mathbf{x})$ are evaluated at the same position; compare Figure 5B. However, if we compute the gradient via forward or backward differences, respectively, this will not be the case. The forward or backward partial derivatives in direction $\mathbf{e}_i$ are not evaluated at $\mathbf{x}$, but at $\mathbf{x} \pm h/2\mathbf{e}_i$, respectively, the faces of the cell. In particular, the partial derivatives in different directions will also be located on different faces. The resulting gradient fields are shown in Figure 5C,D, respectively. Both appear deformed and uneven compared with the central differences approach. Furthermore, a diagonal offset is noticeable. Numerical tests show that, in our present setting, the gradient approximation based on central differences is more accurate than the other approaches and will therefore be preferred; see also Section 4.2.

3.4 | Computing Minkowski tensors

In this section, we propose formulae for computing the volume (fraction) of Ω_1, the surface area of $\partial\Omega_1$, and the Minkowski tensor $W_1^{0,2}(\Omega_1)$. Their accuracy and multigrid convergence will be investigated by numerical means in Section 4.2. The volume is approximated by quadrature, more precisely, by the trapezoidal rule, via

$$V(\Omega_1) \approx \sum_{\mathbf{x} \in Y_h} \chi_h(\mathbf{x}) h^3. \tag{3.1}$$

Motivated by results from geometric measure theory, compare Giusti[63] (Defintion 1.6, Theorem 1.24 and Definition 3.3) and Maggi[64] (Proposition 12.20), we approximate the surface area via

$$S(\Omega_1) \approx \sum_{\mathbf{x} \in Y_h} \|\mathbf{g}(\mathbf{x})\| h^3, \tag{3.2}$$

(A) Filtered image $\mathcal{I}_h^\sigma$ (B) $\|\nabla_h \mathcal{I}_h^\sigma\|$, computed via (C) $\|\nabla_h \mathcal{I}_h^\sigma\|$, computed via (D) $\|\nabla_h \mathcal{I}_h^\sigma\|$, computed via
forward differences   backward differences   central differences
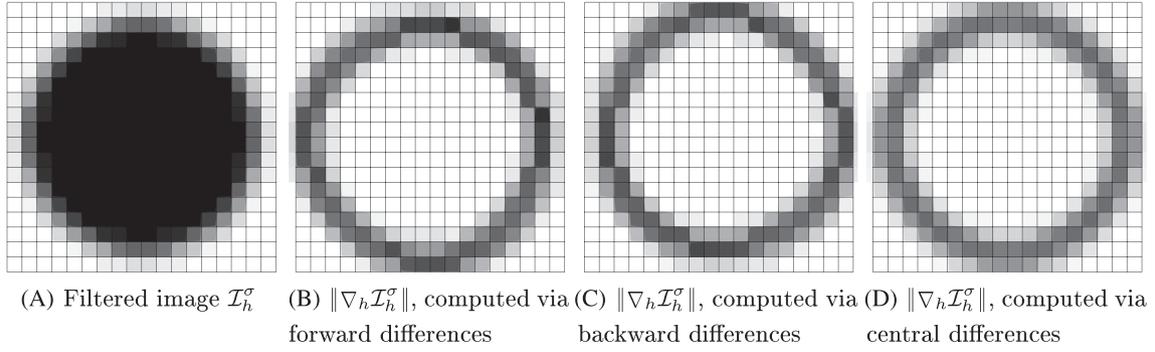
FIGURE 5 Filtered gray value image of a ball (A) and norm of the gradient computed via the three different finite difference approximations (B)–(D)

where the gradient $\mathbf{g}(\mathbf{x})$ is computed by finite differences and $\|\cdot\|$ denotes the Euclidean norm. Due to the relation $S(\Omega_1) = 3\mathrm{tr}(W_1^{0,2}(\Omega_1))$, we approximate the Minkowski tensor $W_1^{0,2}$ by

$$W_1^{0,2}(\Omega_1) \approx \frac{1}{3} \sum_{\mathbf{x} \in Y_h} \mathbf{g}(\mathbf{x}) \otimes \mathbf{g}(\mathbf{x}) \frac{h^3}{\|\mathbf{g}(\mathbf{x})\| + \epsilon}, \tag{3.3}$$

where $\epsilon > 0$ is a small constant used to avoid division by zero. The approximation of the QNT is computed from the approximation of $W_1^{0,2}$ by dividing by the trace, as in its definition (2.6).

4 | NUMERICAL EXAMPLES

4.1 | Setup

The algorithms 1 and 2 (as well as algorithm 3 discussed in Section 4.3 below) were implemented in Python 3.7 with Cython[65] extensions. Critical operations were parallelized using OpenMP. For the eigenvalue decomposition of the structure tensor, discussed in Section 4.3 below, we rely on LAPACK.[66] The computations were performed on a desktop computer with a 6-core Intel i7 CPU and 32GB RAM.

4.2 | Parameter selection and multigrid convergence

The proposed algorithm depends on several basic parameters including the grid size, the gray scale depth, the type and width of the applied filter, and the choice of the gradient approximation, which we are free to choose in order to tune the algorithm. In this section, we investigate the influence of these parameters and propose suitable choices.

In practical applications, the continuous range [0, 1] of gray values is replaced by a set of discrete colors

$$C^p = \begin{cases} \{0, 1\} & \text{if } p = 1, \\ \{0, \frac{1}{p^3-1}, \frac{2}{p^3-1}, \ldots, 1\} & \text{if } p \geq 2 \end{cases}$$

of depth $p \geq 1$. In this context, we consider the discrete characteristic function as the mapping $\chi_h : Y_h \to C^p$. For $p = 1$, we voxelize the object under consideration in a binary manner, by colorizing a voxel if its center lies inside the object. For $p > 1$, we compute the binary image on the finer grid $h' = h/p$ and determine the gray value of a voxel of size h as the mean value of its p^3 subvoxels, resulting in a gray value image of depth p. We investigate a ball B_R of radius $R > 0$ for different p. The Minkowski quantities of B_R are known exactly and given by

$$V(B_R) = \frac{4\pi R^3}{3}, \quad S(B_R) = 4\pi R^2, \quad W_1^{0,2}(B_R) = \frac{4\pi R^2}{9}\mathrm{Id}, \quad \mathrm{QNT}(B_R) = \frac{1}{3}\mathrm{Id};$$

see Appendix A.1 for a derivation of the expressions for $W_1^{0,2}$ and QNT. Hence, these quantities can be compared with the corresponding numerically determined quantities $V^\approx$, $S^\approx$, $W^\approx = W_1^{0,2,\approx}$, and $\mathrm{QNT}^\approx$. For $W = W_1^{0,2}$ and QNT, we define

error measures by

$$E = \frac{\|W(B_R) - W^{\approx}(B_R)\|}{\|W(B_R)\|} \quad \text{and} \quad \overline{E} = \frac{\|QNT(B_R) - QNT^{\approx}(B_R)\|}{\|QNT(B_R)\|},$$

where $\| \cdot \|$ denotes the Frobenius norm. Since W is connected to the surface area via $S = 3\text{tr}(W)$, the error E is directly affected by an error in computing S. In contrast, this latter error does not necessarily affect $\overline{E}$, as both QNT and QNT$^{\approx}$ have trace 1.

We investigate the influence of the different gradient approximations, filter kernels, and filter widths σ, as well as that of the depth p of the initial gray value image, and we examine multigrid convergence as $h \to 0$ numerically. The effect of

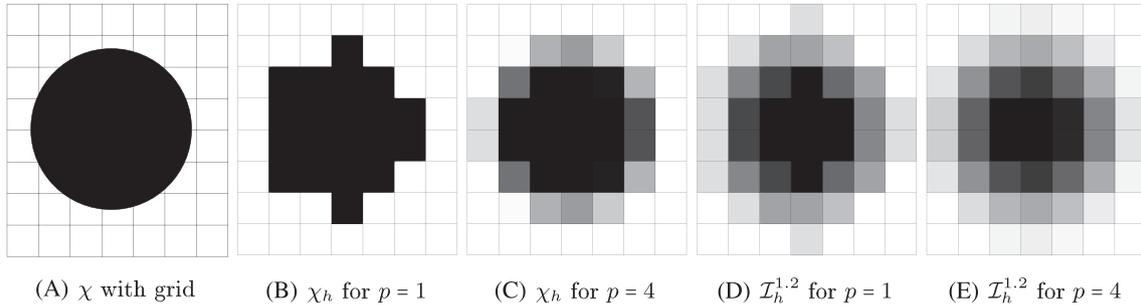(A) χ with grid   (B) χ_h for $p = 1$ (C) χ_h for $p = 4$ (D) $\mathcal{I}_h^{1.2}$ for $p = 1$ (E) $\mathcal{I}_h^{1.2}$ for $p = 4$

FIGURE 6 Characteristic function χ, discrete characteristic function χ_h, and filtered image $\mathcal{I}_h^{1.2}$ for a single ball using depths 1 and 4

(A) volume fraction   (B) total surface area

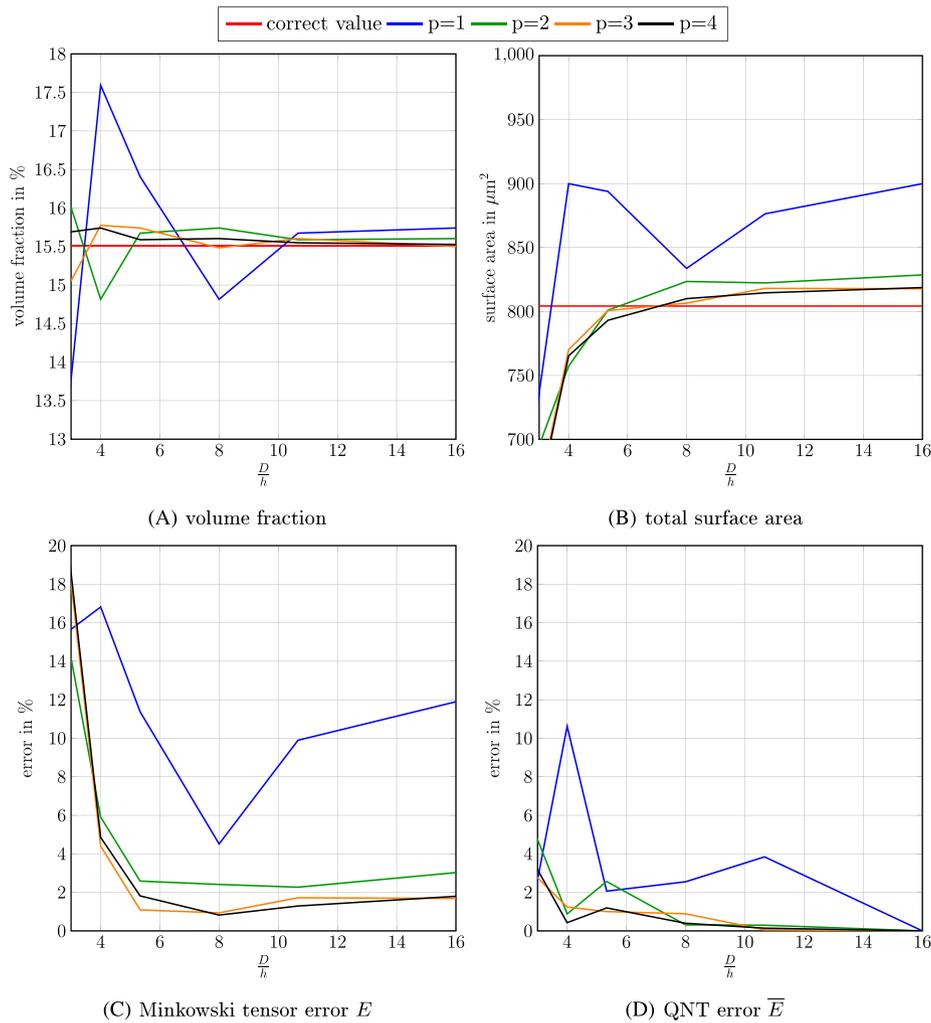(C) Minkowski tensor error E (D) QNT error $\overline{E}$

FIGURE 7 Volume fraction, total surface area, and tensor errors E and $\overline{E}$ for the unfiltered image, thta is, $\sigma = 0$. The gradient was computed via central differences [Colour figure can be viewed at wileyonlinelibrary.com]

the filters on the initial gray value image, depending on the image depth, is exemplified in Figure 6. In Figure 6A, we see a slice through the characteristic function of a ball with a regular grid in the background. In Figure 6B,C, we see slices of the discrete characteristic functions of the ball for depths 1 and 4. The center of the ball does not lie in the center of a voxel but was chosen with a slight displacement, which results in a more uneven representation of the ball in the discrete images compared with Figure 3.

Apparently, images with a higher depth give rise to a more accurate representation of a ball than binary images do. Figure 6D,E shows the image after applying a ball-filter with $\sigma = 1.2$. We see that the difference between depths 1 and 4 has become smaller but remains visible. The filtered binary image ($p = 1$) seems more uneven than the filtered gray-scale image ($p = 4$).

First, we study the influence of the gray value depth p of the initial voxel image for different spatial resolutions. The structure under consideration contains a single ball of diameter 16 μm in a box of edge length 24 μm, that is, the material has a volume fraction of 15.5%. For this first study, we omit using a filter and rely on central differences for the gradient estimation.

Figure 7A shows the computed volume fraction versus D/h, the diameter of the ball per voxel length, for several gray value depths p. The binary image, that is, $p = 1$, exhibits the largest error and oscillates around the correct value. Only for a high resolution above $D/h = 10$, the error is within reasonable bounds. For a higher depth, the volume fraction is accurate even for the lowest resolution.

The computed surface area versus D/h is shown in Figure 7B. Using the binary image without any filter overestimates, the surface area significantly and does not converge. For $p \geq 2$, we see that the error is reasonable for a resolution of 4 voxels per diameter and higher. For higher resolution and higher depth, the surface area computation is rather accurate but systematically overestimates the correct value by about 2% and does not converge. The error E of the Minkowski tensor is shown in Figure 7C. For $p \geq 2$, it is below 6% even for the second-coarsest resolution of $D/h = 4$ and stays below 3% at higher resolutions. Finally, the QNT is the one among the computed characteristics which is computed most accurately; see Figure 7D. For $p \geq 2$, the error is below 5% for all spatial resolutions. Additionally, for all image depths, multigrid convergence is visible. This suggests that, to some degree, the error of computing the Minkowski tensor results from the mentioned overestimation of the surface area. Indeed, since QNT differs from $W_1^{0,2}$ by its trace and $\text{tr}(W_1^{0,2}) = S/3$, the error of computing the surface area present in $W_1^{0,2}$ cancels out to some extent in QNT.

In a second series of numerical experiments, we repeated large parts of the above tests using first-order gradient approximations, as described in Section 3.3, instead of central differences. Compared with the latter, both first-order gradient approximations induce much larger errors, exceeding 20%. Therefore, we will restrict to central differences for the remainder of the article.

Finally, we examine the influence of different filter kernels. Figure 8 shows the surface area as well as the two tensor-error measures versus D/h for gray value depth $p = 1$ (binary) on the left and $p = 3$ on the right. We consider the ball filter $\mathcal{B}_\sigma$ and the Gaussian filter $\mathcal{G}_\sigma$, both with filter parameters $\sigma = 1.2$ and $\sigma = 2$, that is, for a filter width slightly larger than a single voxel and a filter width of 2 voxels.

In general, the errors for the gray value image are smaller compared with the binary image. Focusing on the surface-area computation, that is, Figure 8A,B, we notice that applying no filter is actually most beneficial for a low spatial resolution. For $p = 3$, this even holds up to $D/h = 10$. For $p = 1$, the surface area is strongly overestimated for higher resolution. Even for $p = 3$, no multigrid convergence is achieved, if the filtering step is skipped. To achieve convergence, the ball filter with $\sigma = 1.2$ is the most accurate. For $p = 1$, the ball filter with $\sigma = 1.2$ appears to be the best choice for resolutions up to $D/h = 10$. Above that threshold, the choice $\sigma = 2$ exhibits the smallest error. Nevertheless, the ball filter with $\sigma = 1.2$ serves as a good compromise. For both gray image depths, applying the ball filter leads to better results than applying the Gaussian filter for computing the surface area of the structure.

Investigating the error E, see Figure 8C,D, permits us to draw similar conclusions. Figure 8E,F shows that the filter choice plays a subordinate role compared with the image depth for the error $\overline{E}$. For the binary image, the Gaussian filter with $\sigma = 2$ exhibits the lowest error, staying below the threshold of 2% for all resolutions. For gray value images, however, the error of computing the QNT is below 3% for all resolutions and filters, which is accurate enough for most applications.

4.3 | A short fiber-reinforced composite

4.3.1 | Characterization of fiber-reinforced composites

Short fiber-reinforced composites enjoy great popularity owing to their high (mass-)specific stiffness.[67] The local fiber alignment is strongly dependent on the manufacturing process.[68] The effective material behavior of short fiber-reinforced
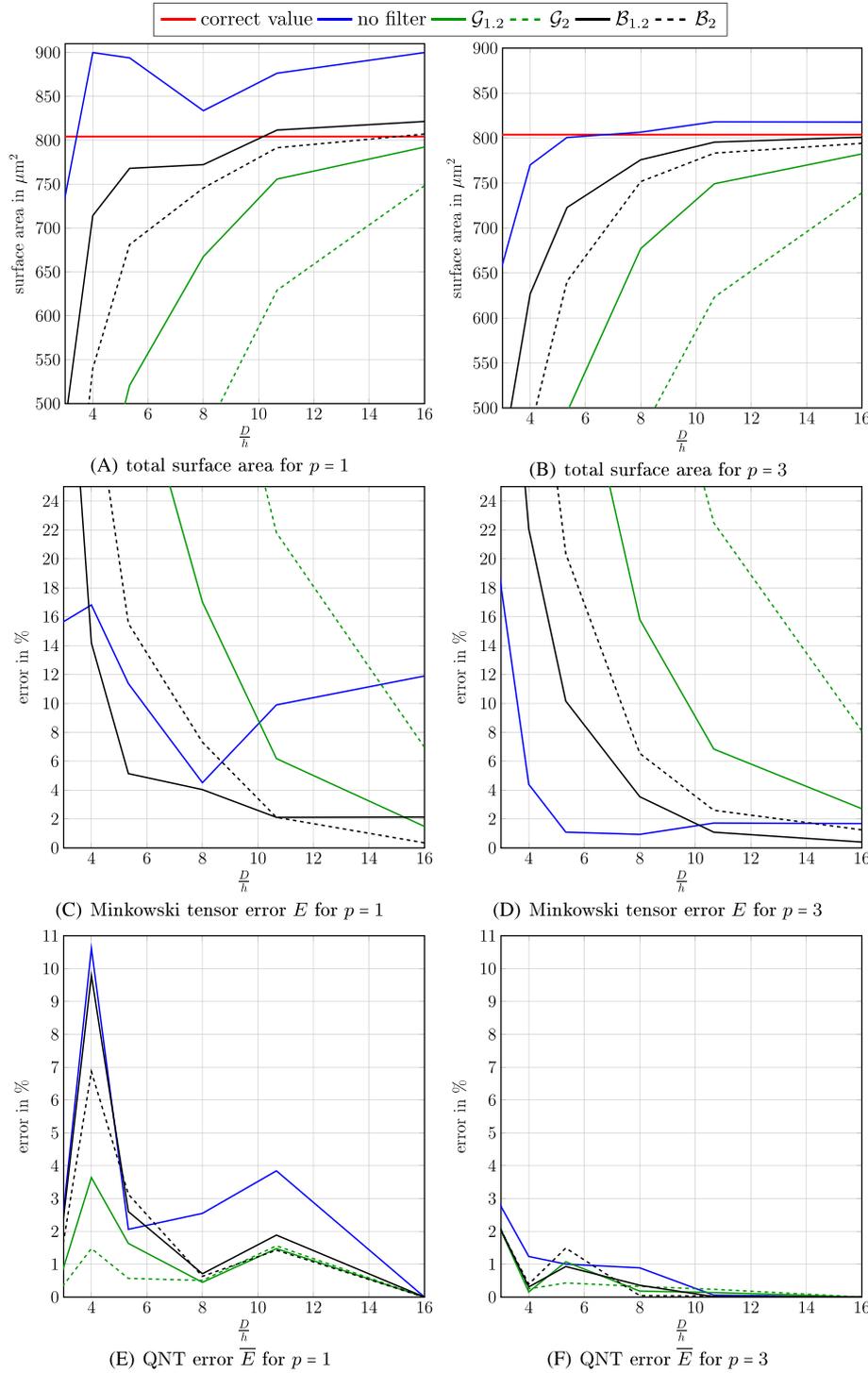
FIGURE 8 Surface area and tensor errors E and $\overline{E}$ for depths $p = 1$ and $p = 3$ comparing the filter choice [Colour figure can be viewed at wileyonlinelibrary.com]

composites is anisotropic, in general, and strongly dependent on the local fiber orientation. Each fiber is interpreted as a straight spherical cylinder of length L and diameter D, axis-aligned with unit vector **p**. Frequently used microstructure characteristics for fiber-reinforced composite materials are the volume fraction, the aspect ratio L/D, and the fiber orientation tensors of second or fourth order.[10,11] For fibers of equal length and equal diameter, the resulting fiber orientation tensors (of order 2 and 4) of a structure with N fibers and orientation vectors $\mathbf{p}_1, \ldots, \mathbf{p}_N$ are defined by

$$A = \frac{1}{N}\sum_{i=1}^{N}\mathbf{p}_i \otimes \mathbf{p}_i \quad \text{and} \quad \mathbb{A} = \frac{1}{N}\sum_{i=1}^{N}\mathbf{p}_i \otimes \mathbf{p}_i \otimes \mathbf{p}_i \otimes \mathbf{p}_i.$$

For varying fiber length and diameter, similar expressions have been proposed in Bay-Tucker[69] based on length- or volume-weighted averaging.

For a gray value μ-CT image, the fiber orientation tensors of second and fourth order may be computed by a variety of methods; see Pinter et al.[70] A popular approach uses the structure tensor[15]; compare Algorithm 3. Alternatively, fibers may be segmented individually; see Hessmann et al[71] for recent work.

To gain insight into the relation between the fiber orientation tensor A and the Minkowski tensor $W_1^{0,2}$, we compare their expressions for a single fiber of length L and diameter D, oriented in direction $\mathbf{p}$; see Appendix A.2 for the detailed computation:

$$A = \mathbf{p} \otimes \mathbf{p}, \tag{4.1}$$

$$W_1^{0,2} = \frac{\pi D^2}{6} \left[\mathbf{p} \otimes \mathbf{p} + \frac{L}{D} (\mathrm{Id} - \mathbf{p} \otimes \mathbf{p}) \right] \text{ and} \tag{4.2}$$

$$\mathrm{QNT} = \frac{1}{1 + 2\frac{L}{D}} \left[\mathbf{p} \otimes \mathbf{p} + \frac{L}{D} (\mathrm{Id} - \mathbf{p} \otimes \mathbf{p}) \right]. \tag{4.3}$$

For microstructures containing N fibers, A is computed by averaging the single-fiber expression (4.1). $W_1^{0,2}$ is computed by summing (4.2) over all fibers. The resulting QNT may be computed as a surface area-weighted average of expression (4.3).

The fiber orientation tensor and the QNT need to be interpreted differently:

- For a single fiber K, the fiber orientation tensor of second order is a singular matrix (of rank 1) describing the projection onto the fiber axis. In contrast, the Minkowski tensor $W_1^{0,2}(K)$ of a single fiber K is a full rank matrix, which arises as a weighted sum of the orthogonal projection onto the fiber axis and the complementary projection onto the plane perpendicular to this axis.

TABLE 1 Comparison of fiber orientation tensor A and quadratic normal tensor QNT for microstructures of different orientation and aspect ratio

	A	QNT for $\frac{L}{D} = 10$	QNT for $\frac{L}{D} = 25$	QNT for $\frac{L}{D} = 50$
#1	$\begin{pmatrix} 1 & 0 & 0 \\ 0 & 0 & 0 \\ 0 & 0 & 0 \end{pmatrix}$	$\begin{pmatrix} 0.048 & 0 & 0 \\ 0 & 0.476 & 0 \\ 0 & 0 & 0.476 \end{pmatrix}$	$\begin{pmatrix} 0.025 & 0 & 0 \\ 0 & 0.4875 & 0 \\ 0 & 0 & 0.4875 \end{pmatrix}$	$\begin{pmatrix} 0.012 & 0 & 0 \\ 0 & 0.494 & 0 \\ 0 & 0 & 0.494 \end{pmatrix}$
#2	$\begin{pmatrix} 0.79 & 0 & 0 \\ 0 & 0.19 & 0 \\ 0 & 0 & 0.02 \end{pmatrix}$	$\begin{pmatrix} 0.1379 & 0 & 0 \\ 0 & 0.3946 & 0 \\ 0 & 0 & 0.4675 \end{pmatrix}$	$\begin{pmatrix} 0.1219 & 0 & 0 \\ 0 & 0.3996 & 0 \\ 0 & 0 & 0.4785 \end{pmatrix}$	$\begin{pmatrix} 0.1131 & 0 & 0 \\ 0 & 0.4024 & 0 \\ 0 & 0 & 0.4845 \end{pmatrix}$
#3	$\begin{pmatrix} 0.49 & 0 & 0 \\ 0 & 0.49 & 0 \\ 0 & 0 & 0.02 \end{pmatrix}$	$\begin{pmatrix} 0.266 & 0 & 0 \\ 0 & 0.266 & 0 \\ 0 & 0 & 0.468 \end{pmatrix}$	$\begin{pmatrix} 0.2607 & 0 & 0 \\ 0 & 0.2607 & 0 \\ 0 & 0 & 0.4785 \end{pmatrix}$	$\begin{pmatrix} 0.258 & 0 & 0 \\ 0 & 0.258 & 0 \\ 0 & 0 & 0.484 \end{pmatrix}$
#4	$\begin{pmatrix} 0.6 & 0 & 0 \\ 0 & 0.3 & 0 \\ 0 & 0 & 0.1 \end{pmatrix}$	$\begin{pmatrix} 0.219 & 0 & 0 \\ 0 & 0.348 & 0 \\ 0 & 0 & 0.433 \end{pmatrix}$	$\begin{pmatrix} 0.21 & 0 & 0 \\ 0 & 0.349 & 0 \\ 0 & 0 & 0.441 \end{pmatrix}$	$\begin{pmatrix} 0.205 & 0 & 0 \\ 0 & 0.349 & 0 \\ 0 & 0 & 0.446 \end{pmatrix}$
#5	$\begin{pmatrix} 0.33 & 0 & 0 \\ 0 & 0.33 & 0 \\ 0 & 0 & 0.33 \end{pmatrix}$	$\begin{pmatrix} 0.333 & 0 & 0 \\ 0 & 0.335 & 0 \\ 0 & 0 & 0.332 \end{pmatrix}$	$\begin{pmatrix} 0.333 & 0 & 0 \\ 0 & 0.335 & 0 \\ 0 & 0 & 0.332 \end{pmatrix}$	$\begin{pmatrix} 0.333 & 0 & 0 \\ 0 & 0.335 & 0 \\ 0 & 0 & 0.332 \end{pmatrix}$

Abbreviation: QNT, quadratic normal tensor.

TABLE 2 The degree of anisotropy of the different structures considered in Table 1 measured by means of the eigenvalue ratio $\beta(\mathrm{QNT})$ of the quadratic normal tensor; compare Equation (2.5)

	β for $\frac{L}{D} = 10$	β for $\frac{L}{D} = 25$	β for $\frac{L}{D} = 50$
#1	0.1003	0.0503	0.0250
#2	0.2943	0.2544	0.2343
#3	0.5690	0.5448	0.5327
#4	0.5055	0.4751	0.4598
#5	0.991	0.9903	0.9899

Note: Apparently, the anisotropy does not only depend on the fiber orientation distribution, but is also sensitive to the aspect ratio L/D of the fibers.

Abbreviation: QNT, quadratic normal tensor.

(A) 1% relative distance

(B) 1% relative distance - slice

(C) 10% relative distance

(D) 10% relative distance - slice

(E) 50% relative distance
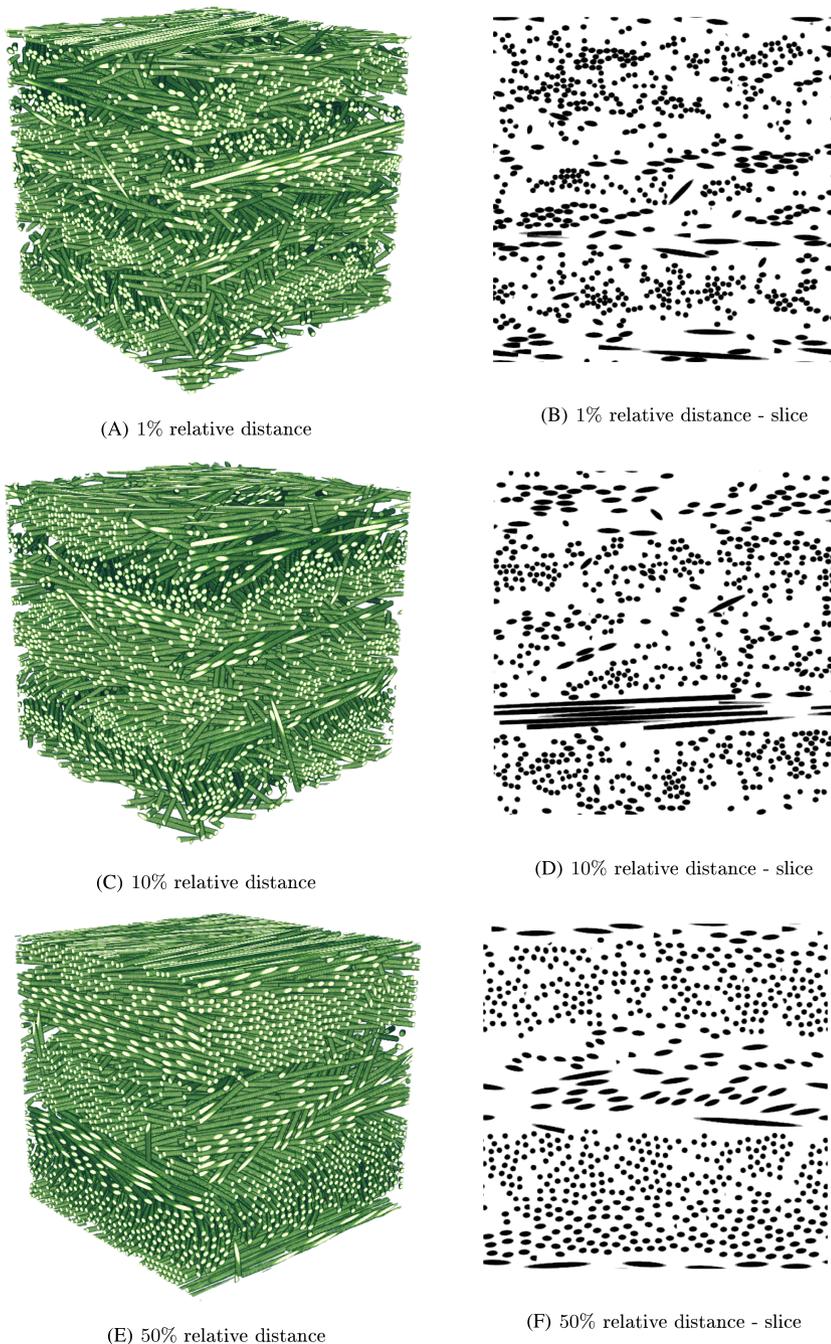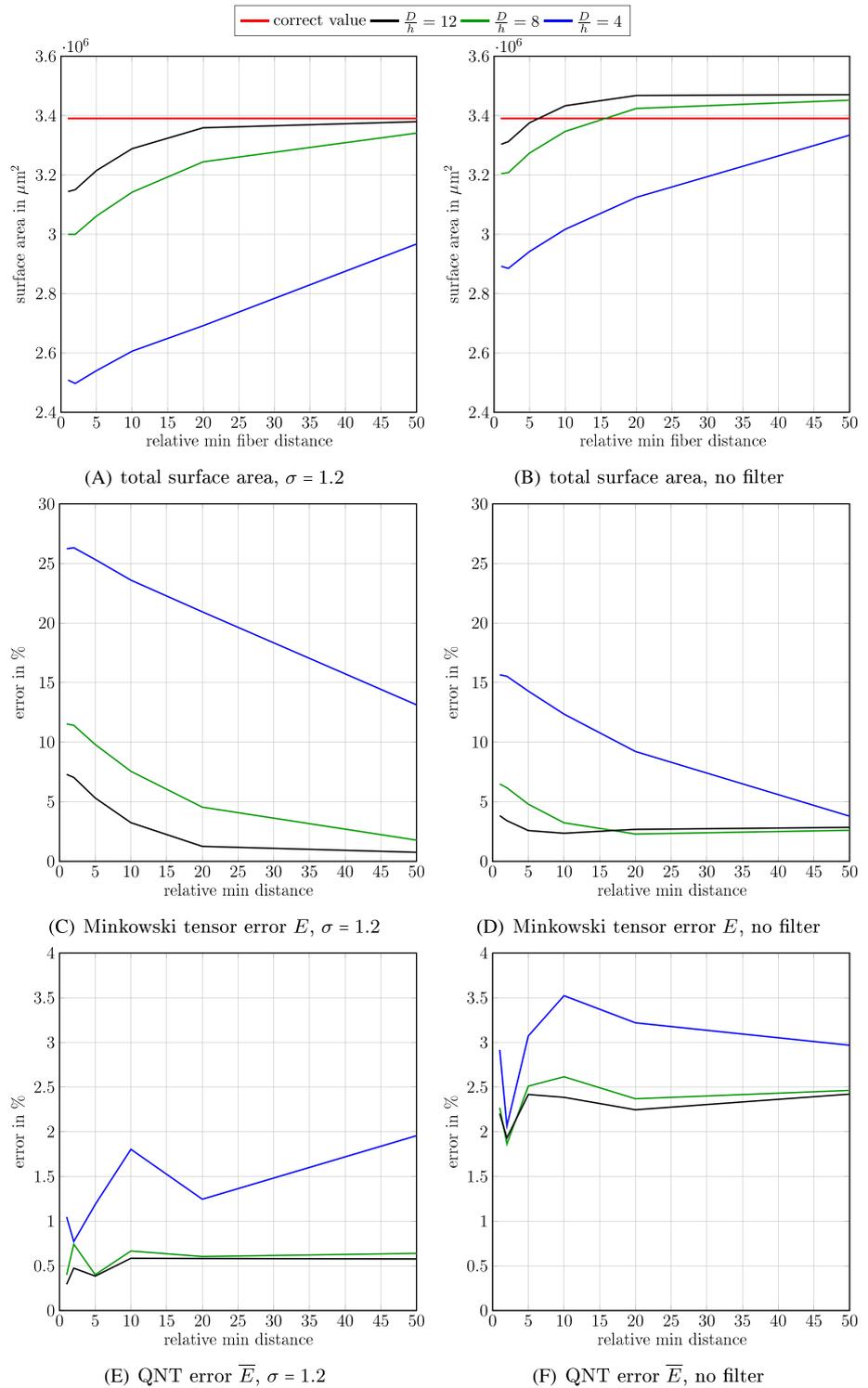

(F) 50% relative distance - slice

FIGURE 9 Fiber-reinforced composite containing 1336 fibers of equal length and varying inter-fiber spacing. The structures were generated synthetically using the sequential addition and migration algorithm.[73] [Colour figure can be viewed at wileyonlinelibrary.com]

- For high aspect ratios, that is, for $L \gg D$, for the QNT, the prefactor in front of the complementary projection is much larger than the other prefactor.
- Using the fiber orientation tensor as a descriptor of a microstructure rests upon specific assumptions that are often not satisfied for real structures. Typically, fibers are not of equal length, because they break during to the manufacturing process.[72] Furthermore, the assumption that fibers are straight cylinders is not met in most of the cases, as longer fibers bend during manufacturing and therefore exhibit curvature.[58] In such situations, the structure tensor-based computation of the fiber orientation tensor still gives *some* tensorial quantity as output. However, interpreting this result as a fiber orientation tensor may not be justified.

The Minkowski tensors, on the other hand, are not restricted to specific geometric assumptions such as particular shapes. Therefore, for structures containing curved fibers of different lengths or mixtures of fibers with other objects, and so on, $W_1^{0,2}$ is still a geometrically well-defined quantity. As Minkowski tensors are integrals of locally computable

(A) total surface area, $\sigma = 1.2$

(B) total surface area, no filter

(C) Minkowski tensor error E, $\sigma = 1.2$

(D) Minkowski tensor error E, no filter

(E) QNT error $\overline{E}$, $\sigma = 1.2$

(F) QNT error $\overline{E}$, no filter

quantities, compare (2.4), they are even well-defined locally on any piece of a complex geometric structure. In contrast, the fiber orientation tensor is a nonlocal quantity intrinsically tied to cylindrical shapes.

An overview of how the fiber orientation tensor compares with the QNT for varying aspect ratios is given in Table 1. For this study, we generated 5×3 different microstructures, each containing 20% fibers of equal length and diameter, using the sequential addition and migration algorithm.[73] This algorithm draws fibers from an angular central Gaussian distributions on the two-dimensional sphere.[74] Indeed, the set of possible angular central Gaussian distributions may be parameterized by the second-order fiber orientation tensors; see Montgomery-Smith et al.[75]
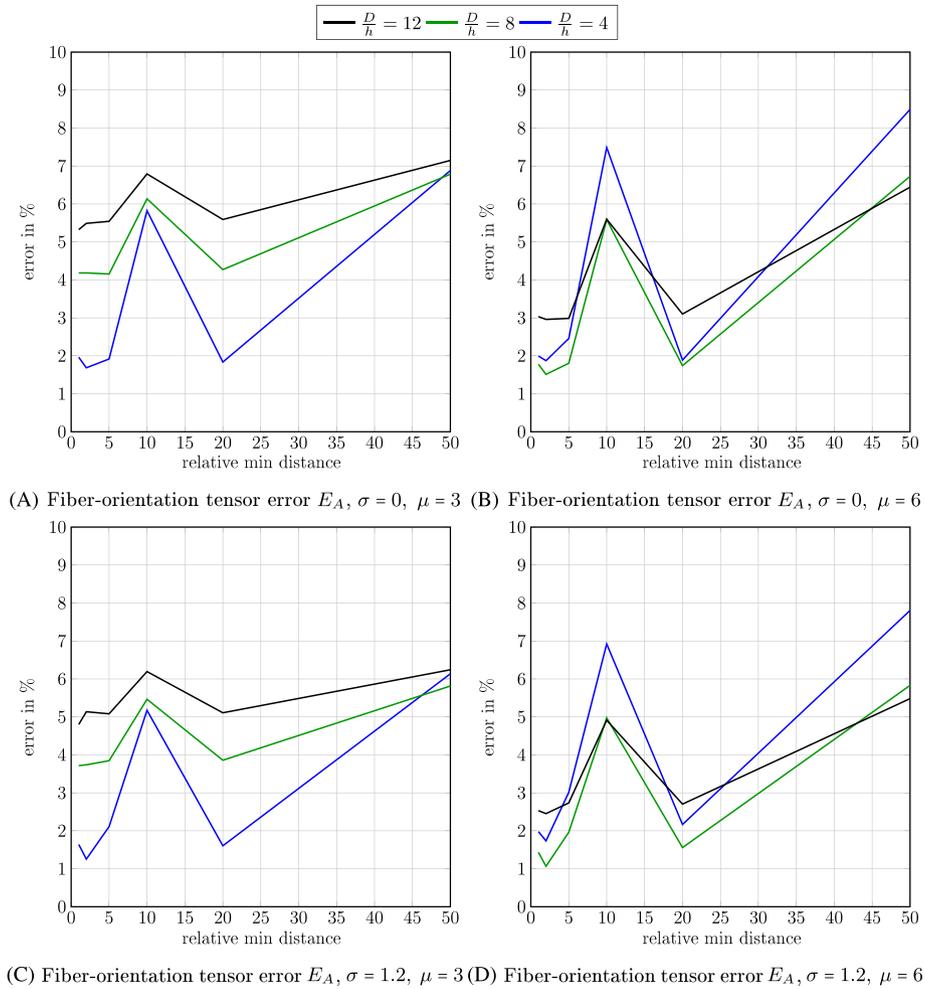
(A) Fiber-orientation tensor error E_A, $\sigma = 0$, $\mu = 3$ (B) Fiber-orientation tensor error E_A, $\sigma = 0$, $\mu = 6$

(C) Fiber-orientation tensor error E_A, $\sigma = 1.2$, $\mu = 3$ (D) Fiber-orientation tensor error E_A, $\sigma = 1.2$, $\mu = 6$

FIGURE 11 Error of the structure tensor-based fiber orientation tensor computation using different filter parameters for the first and second filters [Colour figure can be viewed at wileyonlinelibrary.com]

Across the microstructures, we varied the orientation distribution (five different ones #1 − #5) and the aspect ratio (three different choices: $L/D = 10, 25,$ and 50). For convenience, all matrices are chosen to be diagonal w.r.t. the standard basis $\{\mathbf{e}_1, \mathbf{e}_2, \mathbf{e}_3\}$.

Microstructure #1 is composed of aligned fibers in e_1-direction. The second microstructure lies almost entirely within the $\mathbf{e}_1 − \mathbf{e}_2$-plane, with preferred direction $\mathbf{e}_1$. The almost planar isotropic case in the $\mathbf{e}_1 − \mathbf{e}_2$-plane is realized via microstructure #3. A general anisotropic case with preferred direction $\mathbf{e}_1$ and least preferred direction $\mathbf{e}_3$ is given in case #4. And, finally, microstructure #5 shows the isotropic case. For the isotropic orientation (#5), all tensors are nearly equal. The QNT for the almost planar orientation (#3) results in one larger (corresponding to the normal vector of the plane) and two equal smaller eigenvalues, indicating no preferred direction within the plane. The QNT of structure #2 exhibits three different eigenvalues. The largest is equal to the largest eigenvalue of #3. Of the two smaller eigenvalues, the smallest indicates a preferred direction. The same interpretation holds for structure #4. For the unidirectional case (#1), the largest eigenvalue appears twice, which indicates a planar symmetry in both planes normal to the corresponding eigenvectors. By the smallest eigenvalue, again, a preferred direction is indicated.

In contrast to the fiber orientation tensor A, the QNT varies also with the aspect ratio L/D of the fibers. This may also be seen from the eigenvalue ratio β of QNT, compare (2.5), listed in Table 2. This scalar measure of anisotropy is smallest in case of a unidirectional orientation distribution (#1) and almost 1 in the isotropic case #5. The degree of anisotropy is amplified for higher aspect ratios, which results in a lower β.

4.3.2 | Sensitivity w.r.t. interfiber spacing

A well-known challenge when computing fiber orientation measures on μ-CT scans is the sensitivity w.r.t. spatial resolution, as well as overlapping or touching fibers.[76] In the following study, we investigate the influence of the interfiber distance.

Using the sequential addition and migration algorithm,[73] we generated structures with 20% fibers of aspect ratio 25, containing a total of 1336 inclusions. The fiber orientation tensor was chosen almost planar isotropic with $A = \text{diag}(0.49, 0.49, 0.02)$. The minimum distance between the fibers compared with their diameter can be chosen as an input for the microstructure generator. We generated six microstructures with minimum relative distance varying from 1% to 50% . Volumetric views and transverse slices of three of these structures are shown in Figure 9. For 1% relative distance, several bundles of touching or almost touching fibers are visible, whereas for 50%, each fiber is comfortably surrounded by matrix material. All structures were voxelized with gray value depth $p = 2$ and for three spatial resolutions of $D/h = 4, D/h = 8$ and $D/h = 12$, resulting in volume images with 256^3, 512^3, and 768^3 voxels, respectively.

For this data set, we compare the surface area computation and the errors for the tensors $W_1^{0.2}$ and QNT. As processing options, we compare no filter and the ball filter $\mathcal{B}_\sigma$ with filter parameter $\sigma = 1.2$. The central difference approximation is used for the gradient.

Figure 10A shows the computed total surface area versus the minimum fiber distance relative to the diameter for the three spatial resolutions under consideration, using the ball filter with $\sigma = 1.2$. We observe two trends. Firstly, the surface area is generally underestimated for all spatial resolutions. However, we clearly see multigrid convergence. Furthermore, the error is smaller for the larger minimum distance. This observation conforms to our expectations, as the surface area of touching or almost touching fibers is not computed accurately enough by a gradient-based approximation. In Figure 10B, we see the results of the surface area computation without applying any filter. The errors are, in general, lower than in the case of $\sigma = 1.2$. However, neither multigrid convergence nor a convergence as the minimum fiber distance increases is observed. Figure 10C,D shows the error E for both filter choices. Again, the results reflect the relative error of the surface area estimation. Figure 10E,F contains the errors of the QNT for both filter choices. For no filter application, the error is below 4%, and for $\sigma = 1.2$, it is even below 2% for all spatial resolutions and minimum interfiber distances. No clear trend w.r.t. the interfiber spacing is visible. Hence, the QNT may serve as a microstructure descriptor that is robust w.r.t. small interfiber spacing.

We compare our approach with the well-established structure tensor method; see Algorithm 3, which we implemented into our code.

Algorithm 3 Computing the fiber orientation tensor via the structure tensor method[15]

1: $\mathcal{I}_h^\sigma \leftarrow \mathcal{F}_\sigma * \chi_h$ ▷ Blur image with image filter
2: $\mathbf{g}(\mathbf{x}) \leftarrow \nabla_h \mathcal{I}_h^\sigma$ ▷ Apply discrete gradient
3: $I(\mathbf{x}) \leftarrow \mathbf{g}(\mathbf{x}) \otimes \mathbf{g}(\mathbf{x})$ ▷ Compute local tensor
4: $I_\mu \leftarrow \mathcal{F}_\mu * I$ ▷ Blur local tensor with second filter
5: $\{\lambda_i(\mathbf{x}), \mathbf{v}_i(\mathbf{x})\} \leftarrow \text{Eig}(I_\mu(\mathbf{x}))$ ▷ Local eigenvalue decomposition (sorted, smallest first)
6: $A^{\approx} = \sum_{\mathbf{x} \in Y_h} \mathbf{v}_1(\mathbf{x}) \otimes \mathbf{v}_1(\mathbf{x})$ ▷ Extract local orientation tensor
7: **return** $A^{\approx}/\text{tr}(A^{\approx})$

Computing the fiber orientation tensor numerically via the structure tensor algorithm requires applying a second filter $\mathcal{F}_\mu$ with filter parameter μ to the tensor field $\mathbf{n}(\mathbf{x}) \otimes \mathbf{n}(\mathbf{x})$ (component-wise, this tensor field denotes said "structure tensor"). Pinter et al[70] recommend that for the filter parameter for the second filter should be larger than for the first filter, which should be rather small. In our case, this is best recovered by choosing the ball filter with small filter parameter (i.e., $\sigma = 1.2$) or no filter (i.e., $\sigma = 0$) as the first filter. For the second filter, we choose a Gaussian kernel $\mathcal{G}_\mu$ with $\mu = 3$ and $\mu = 6$. To evaluate the accuracy of the method, we introduce the fiber orientation tensor error measure (similar to $\overline{E}$)

$$E_A = \frac{\|A - A^{\approx}\|}{\|A\|},$$

where $A^{\approx}$ is the approximated fiber orientation tensor computed by the structure tensor approach.

Figure 11 shows the error of this method for the four filter combinations $\sigma = 0, 1.2$; $\mu = 3, 6$. The error is below 9% for all structures and resolutions. The first filter width $\sigma = 1.2$ results in a lower error than for $\sigma = 0$. This holds for all spatial resolutions and fiber distance thresholds. For the second filter, however, the optimal choice depends on the spatial resolution. The two finer resolutions benefit from a larger second filter and even exhibit a larger error for the smaller μ
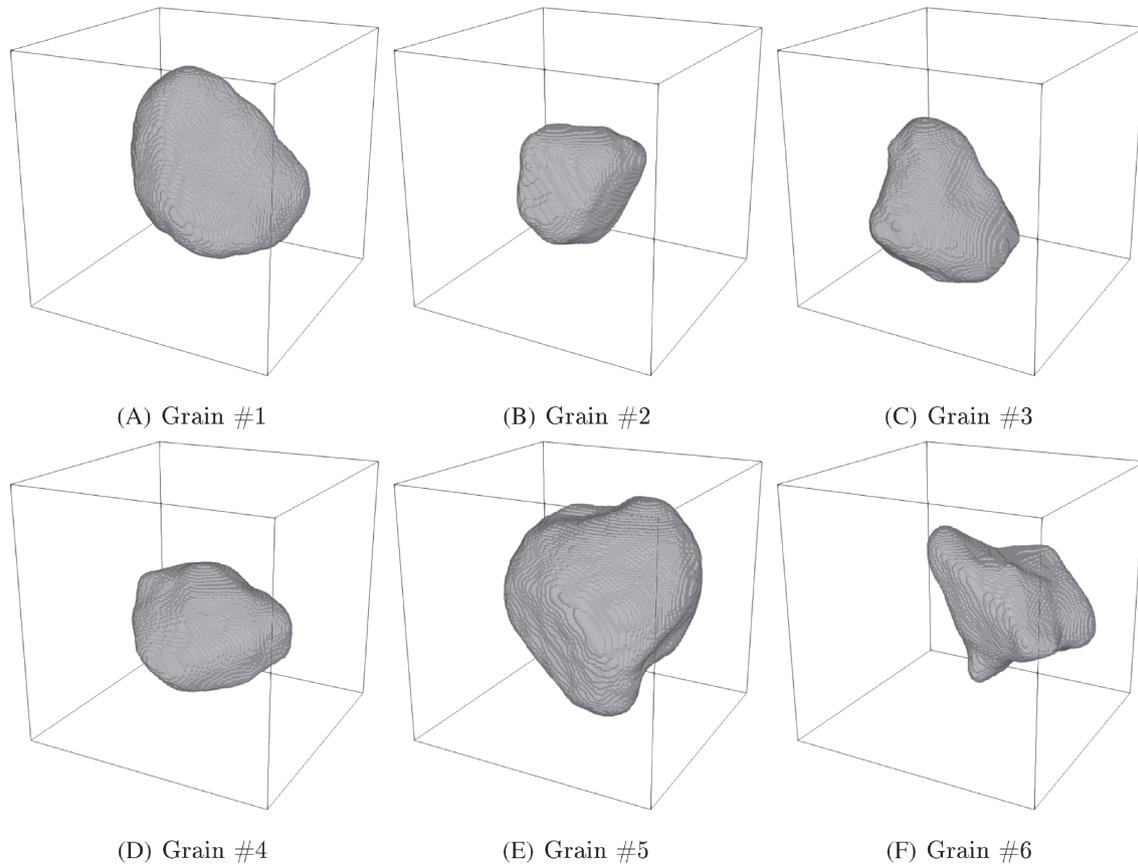
(A) Grain #1   (B) Grain #2   (C) Grain #3

(D) Grain #4   (E) Grain #5   (F) Grain #6

FIGURE 12 Six different sand grains whose shapes are analyzed using QNT; see Table 3

TABLE 3 Quadratic normal tensor QNT and eigenvalue ratio β of the six grains in Figure 12

| Grain	QNT	β	Grain	QNT	β
#1	$\begin{pmatrix} 0.2743 & 0.0518 & 0.0722 \\ 0.0518 & 0.2486 & 0.0179 \\ 0.0722 & 0.0179 & 0.4772 \end{pmatrix}$	0.4044	#2	$\begin{pmatrix} 0.3669 & -0.0428 & 0.0405 \\ -0.0428 & 0.2949 & -0.0204 \\ 0.0405 & -0.0204 & 0.3382 \end{pmatrix}$	0.6643
#3	$\begin{pmatrix} 0.382 & 0.0405 & 0.0055 \\ 0.0405 & 0.2945 & -0.0462 \\ 0.0055 & -0.0462 & 0.3235 \end{pmatrix}$	0.626	#4	$\begin{pmatrix} 0.2195 & 0.0407 & 0.0319 \\ 0.0407 & 0.3979 & 0.0936 \\ 0.0319 & 0.0936 & 0.3826 \end{pmatrix}$	0.4244
#5	$\begin{pmatrix} 0.28 & 0.0092 & 0.0013 \\ 0.0092 & 0.2875 & 0.07 \\ 0.0013 & 0.07 & 0.4325 \end{pmatrix}$	0.5564	#6	$\begin{pmatrix} 0.3123 & 0.07 & 0.0428 \\ 0.07 & 0.3202 & -0.023 \\ 0.0428 & -0.023 & 0.3674 \end{pmatrix}$	0.5795

Abbreviation: QNT, quadratic normal tensor.

than for the coarse resolution. With respect to the relative minimum distance of fibers, no clear trend is visible. The error fluctuates between 1% and 8% for the different microstructures. The error of the QNT, on the other hand, was below 2% for all spatial resolutions and hence provides a reliable option for characterizing fiber-reinforced composites.

All computations were performed in a matter of minutes.

4.4 | Sand grains and sand binder composites

For manufacturing parts with complex geometry, casting is often the preferred choice.[77] For casting, the mold enters a cavity of the specified shape. This cavity, in turn, is realized as a sand core, which has to be destroyed after the casting process. Such sand cores are composed of sand grains which are held together by an organic or inorganic binder. These constituents, their proportion and shape, strongly influence the overall material behavior of the sand binder aggregate.[78] Loosely speaking, if the strength of the aggregate is too low, the part will not survive the casting process. On the other hand, excessive strength may prevent the part to be extracted unscathed from the sand core.
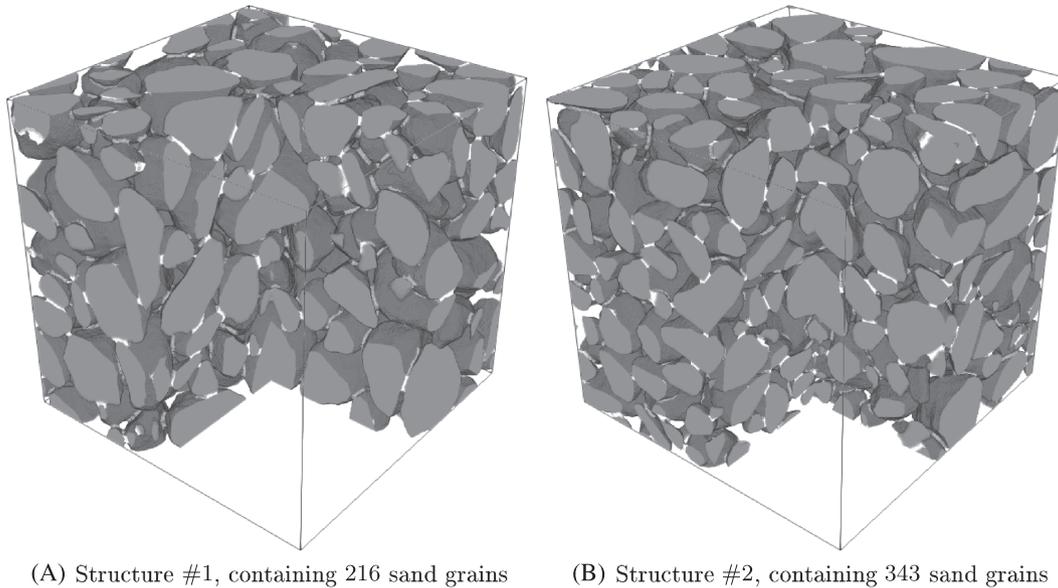
(A) Structure #1, containing 216 sand grains (B) Structure #2, containing 343 sand grains

FIGURE 13 Sand core structures, containing 58.58% sand and 1.28% inorganic binder. The structures were generated by the mechanical contraction method.[78]

TABLE 4 Quadratic normal tensor, degree of anisotropy, and total surface area for grain structures #1 and #2 with and without binder

	Sand grains alone			Sand binder composite		
	QNT	β	S[mm²]	QNT	β	S[mm²]
Structure #1	$\begin{pmatrix} 0.3294 & -0.0002 & -0.0025 \\ -0.0002 & 0.3412 & -0.0094 \\ -0.0025 & -0.0094 & 0.3293 \end{pmatrix}$	0.9329	51.74	$\begin{pmatrix} 0.3292 & -0.0015 & -0.0006 \\ -0.0015 & 0.3396 & -0.0074 \\ -0.0006 & -0.0074 & 0.3312 \end{pmatrix}$	0.9485	47.26
Structure #2	$\begin{pmatrix} 0.3218 & -0.0004 & -0.0011 \\ -0.0004 & 0.3366 & -0.0028 \\ -0.0011 & -0.0028 & 0.3415 \end{pmatrix}$	0.9385	80.72	$\begin{pmatrix} 0.3233 & -0.001 & -0.0014 \\ -0.001 & 0.3362 & -0.0026 \\ -0.0014 & -0.0026 & 0.3405 \end{pmatrix}$	0.9451	73.96

Abbreviation: QNT, quadratic normal tensor.

In this section, we compute the QNT of sand cores to study their anisotropy and to demonstrate the wide range of applicability of quadratic normal tensors. We consider six different sand grain shapes which were obtained from fitting cleaned up and binarized μ-CT scans.[78] The individual grains are shown in Figure 12.

These sand grains are nonconvex and anisotropic. The computed QNT are listed in Table 3. For the computation, we chose the ball filter $\mathcal{B}_\sigma$ with $\sigma = 1.2$ voxels and used central differences for the gradient approximation.

In addition to the QNT, we quantify the degree of anisotropy by listing the eigenvalue ratios (2.5) of QNT. We observe that all sand grains have a distinct degree of anisotropy, varying between $\beta = 0.4$ and $\beta = 0.63$. To gain further insight into the anisotropy of the grains, we compute the eigenvalue decomposition of QNT for grain #1. The eigensystem reads

$$\lambda_1 = 0.5046, \mathbf{v}_1 = \begin{pmatrix} -0.3233 \\ -0.1308 \\ -0.9372 \end{pmatrix}; \quad \lambda_2 = 0.2914, \mathbf{v}_2 = \begin{pmatrix} -0.6666 \\ -0.6715 \\ 0.3236 \end{pmatrix}; \quad \lambda_3 = 0.204, \mathbf{v}_3 = \begin{pmatrix} -0.6717 \\ 0.7294 \\ 0.1299 \end{pmatrix}.$$

The largest eigenvalue indicates a somewhat disc-like shape within the plane normal to $\mathbf{v}_1$. The vectors $\mathbf{v}_2$ and $\mathbf{v}_3$ lie in that plane; the lower eigenvalue λ_3 indicates a slight extension in direction $\mathbf{v}_3$. For a better understanding, we point at Table 1, where fiber-reinforced composites are analyzed and a "translation" to well-known orientation tensors is provided.

These six sand grains of Figure 12 were used for generating sand binder composite microstructures, characteristic for casting applications, using the mechanical contraction method.[78] Two realizations, containing 216 and 343 sand grains, are shown in Figure 13. Both structures consist of 58.58% sand grains and 1.28% inorganic binder. In contrast to particle-filled composites, these microstructures involve an interpenetrating porous phase.

On μ-CT images of sand binder composites, the binder phase cannot be distinguished from the sand phase; compare Schneider et al.[78] Therefore, we investigate how the presence of the binder phase affects the Minkowski tensors. We compare the QNT of the sand binder composite to the one with only sand grains for both structures in Figure 13. We chose the ball filter $\mathcal{B}_\sigma$ with $\sigma = 1.2$ voxels and central differences for the gradient approximation. For all structures, the resulting tensor QNT, the degree of anisotropy β and the total surface area are listed in Table 4.

The QNT is almost isotropic in all four cases. Removing the binder phase leads to slightly more anisotropic QNTs compared with the sand binder composite. However, the change is marginal. Without the binder, the surface area of every grain is fully exposed, which results in a 9.5% larger total surface area in case of structure #1 and 9.1% larger surface area in case of structure #2. In general, we see that, although the grains within both structures are highly anisotropic, the resulting microstructure as a whole is almost isotropic. Hence, mechanical contraction of anisotropic shapes results in an overall isotropic microstructure. This conforms to the results of Schneider et al,[78] where elastic homogenization studies on similar structures were performed. An isotropic approximation of the effective stiffness tensor was shown to be accurate.

5 | CONCLUSION AND OUTLOOK

In this study, we proposed using Minkowski tensors, a tensor-valued generalization of the scalar-valued Minkowski functionals, for the analysis of microstructures given implicitly on voxel images. Due to their tensorial nature, Minkowski tensors naturally contain information about the anisotropy of geometric structures and can be incorporated into continuum mechanical or other physical modeling approaches.

We provide an efficient and compact algorithm for computing the Minkowski tensor $W_1^{0,2}$ and the resulting QNT from 3D gray value image data. This algorithm is based on image filtering and a numerical gradient computation. We demonstrated the multigrid convergence of our algorithm on a single-ball structure. Central differences and a ball filter with low filter parameter turned out to be the most accurate for binary images. For gray value images of low resolution, skipping the filtering step may be beneficial. Furthermore, we demonstrated that the QNT is rather insensitive to errors in the surface area computation, thus providing a robust measure of microstructure anisotropy.

For fiber-reinforced composites, we compared characterizations based on the QNT to the well-established fiber orientation tensors. We compared our approach to the common structure tensor approach and demonstrated the accuracy and robustness of the QNT.

Finally, we studied the QNT of sand core microstructures. Its applicability to complex grain geometries demonstrates the versatility of the Minkowski tensor approach.

In future applications, further Minkowski tensors may be used for describing and characterizing a variety of microstructures, including curved fibers, fibers of different length and diameter, mixtures of several different shapes within a matrix, or polycrystalline structures. For a robust curvature approximation technique based on voxel image data, for instance, the curvature-dependent Minkowski tensor $W_2^{0,2}$ may be computed, providing additional information on the microstructure.

The Minkowski tensors of the second rank may reflect only three types of material symmetries: isotropy, transverse isotropy, and orthotropy. To detect finer material symmetries, working with higher-order Minkowski tensors is necessary. Mickel et al[79] suggested using irreducible Minkowski tensors for anisotropy characterization, a decomposition of the surface normal density into those of some basic shapes in the spirit of Fourier analysis. This approach may also be beneficial for fiber orientation analysis. Moreover, the concept of Minkowski maps[80,81] may allow studying the local differences of the fiber orientation across an inhomogeneous medium.

Last but not the least, Minkowski tensors may serve as input for further studies. Similar to fiber orientation tensor-based mean field models,[82,83] models based on Minkowski tensors may be developed. The QNT is able to provide insights for structures containing curved fibers and may serve as a tool for investigating their mechanical behavior.

CONFLICT OF INTEREST

The authors declare that they have no known competing financial interests or personal relationships that could have appeared to influence the work reported in this paper.

ORCID

Matti Schneider https://orcid.org/0000-0001-7017-3618

REFERENCES

1. Matouš K, Geers MGD, Kouznetsova VG, Gillman A. A review of predictive nonlinear theories for multiscale modeling of heterogeneous materials. *J Comput Phys*. 2017;330:192-220.
2. Schladitz K, Büter A, Godehardt M, et al. Non-destructive characterization of fiber orientation in reinforced SMC as input for simulation based design. *Compos Struct*. 2017;160:195-203.
3. Cnudde V, Cwirzen A, Massachaele B, Jacobs PJS. Porosity and microstructure characterization of building stones and concretes. *Eng Geol*. 2009;103:76-83.
4. Voigt W. Ueber die Beziehung zwischen den beiden Elasticitätsconstanten isotroper Körper. *Annalen der Physik*. 1889;274:573-587.
5. Reuss A. Berechnung der Fließgrenze von Mischkristallen auf Grund der Plastizitätsbedingung für Einkristalle. *ZAMM - Zeitschrift für Angewandte Mathematik und Mechanik*. 1929;9:49-58.
6. Torquato S. *Random Heterogeneous Materials*, Vol. 16. New York: Springer; 2002.
7. Brown WF. Solid Mixture Permittivities. *J Chem Phys*. 1955;23:1514-1517.
8. Torquato S, Stell G. Microstructure of two-phase random media. I. The n-point probability functions. *J Chem Phys*. 1982;77:2071-2077.
9. Eriksen HK, Lilje PB, Branday AJ, Górski KM. Estimating N-Point Correlation Functions from Pixelized Sky Maps. *Astrophys J Suppl Ser*. 2004;151:1-11.
10. Kanatani K. Distribution of directional data and fabric tensors. *Int J Eng Sci*. 1984;22:149-164.
11. Advani SG, Tucker CL. The Use of Tensors to Describe and Predict Fiber Orientation in Short Fiber Composites. *J Rheol*. 1987;31:751-784.
12. Müller V, Böhlke T. Prediction of effective elastic properties of fiber reinforced composites using fiber orientation tensors. *Compos Sci Technol*. 2016;130:36-45.
13. Robb K, Wirjadi O, Schladitz K. Fiber orientation estimation from 3d image data: Practical algorithms, visualization, and interpretation. In: 7th international conference on hybrid intelligent systems (his 2007); 2007:320-325.
14. Daniels F, ter Haar Romenij BM, Rubbens MP, van Assen HC. Quantification of Collagen Orientation in 3D Engineered Tissue. *3rd Kuala Lumpur International Conference on Biomedical Engineering 2006*. Berlin, Heidelberg: Springer; 2007:282-286.
15. Krause M, Hausherr JM, Burgeth B, Herrmann C, Krenkel W. Determination of the fibre orientation in composites using the structure tensor and local X-ray transform. *J Mater Sci*. 2010;45:888-896.
16. Neumann M, Hirsch C, Stanek J, Benes V, Schmidt V. Estimation of geodesic tortuosity and constrictivity in stationary random closed sets. *Scandinavian J Stat*. 2019;46:848-884.
17. Matheron G. *Random Sets and Integral Geometry*: John Wiley & Sons; 1975.
18. Kate JM, Gokhale CS. A simple method to estimate complete pore size distribution of rocks. *Eng Geol*. 2006;84:48-69.
19. Bansal RK, Kubis A, Hull R, Fitz-Gerald JM. High-resolution three-dimensional reconstruction: A combined scanning electron microscope and focused ion-beam approach. *J Vacuum Sci Technol B*. 2006;24(2):554-561.
20. Groeber MA, Haley BK, Uchic MD, Dimiduk DM, Ghosh S. 3D reconstruction and characterization of polycrystalline microstructures using a FIB-SEM system. *Mater Charact*. 2006;57(4):259-273.
21. Zaefferer S, Wright SI, Raabe D. Three-dimensional orientation microscopy in a focused ion beam-scanning electron microscope: A new dimension of microstructure characterization. *Metall Mater Trans A*. 2008;39(2):374-389.
22. Korte S, Ritter J, Jiao C, Midgley PA, Clegg WJ. Three-dimensional electron backscattered diffraction analysis of deformation in MgO micropillars. *Acta Materialia*. 2011;59(19):7241-7254.
23. Adams B, Olson T. The mesostructure - property linkage in polycrystals. *Prog Mater Sci*. 1998;43(1):1-87.
24. Larsen BC, Yang W, Ice GE, Budai JD, Tischler JZ. Three-dimensional X-ray structural microscopy with submicrometre resolution. *Nature*. 2002;415(6874):887-890.
25. Döbrich CM, Rau C, Krill III CE. Quantitative characterization of the three-dimensional microstructure of polycrystalline Al-Sn using X-ray microtomography. *Metall Mater Trans A*. 2004;35(7):1953-1961.
26. Bunge HJ. *Texture Analysis in Materials Science: Mathematical Methods*. London: Butterworth & Co; 1982.
27. Böhlke T. Texture simulation based on tensorial Fourier coefficients. *Comput Struct*. 2006;84:1086-1094.
28. Böhlke T, Lobos M. Representation of Hashin-Shtrikman Bounds of cubic crystal aggregates in terms of texture coefficients with application in materials design. *Acta Materialia*. 2014;67:324-334.
29. Junk M, Budday J, Böhlke T. On the solvability of maximum entropy moment problems in texture analysis. *Math Models Methods Appl Sci*. 2012;12:1250043.
30. Böhlke T, Jöchen K, Kraft O, Löhe D, Schulze V. Elastic properties of polycrystalline microcomponents. *Mech Mater*. 2010;42:11-23.
31. Kozlov SM. The averaging of random operators. *Mat Sb (NS)*. 1979;109(2):188-202.

32. Papanicolaou GC, Varadhan SRS. Boundary value problems with rapidly oscillating random coefficients. *Random Fields, Vol. I, II (Esztergom, 1979)*, Colloq. Math. Soc. János Bolyai, vol. 27. Amsterdam-New York: North-Holland; 1981:835-873.

33. Kanit T, Forest S, Galliet I, Mounoury V, Jeulin D. Determination of the size of the representative volume element for random composites: Statistical and numerical approach. *Int J Solids Struct*. 2003;40:3647-3679.

34. Schneider R, Weil W. *Stochastic and Integral Geometry*. Berlin Heidelberg: Springer; 2008.

35. Hadwiger H. Beweis eines Funktionalsatzes für konvexe Körper. *Abhandlungen aus dem Mathematischen Seminar der Universität Hamburg*. 1951;17:69-76.

36. Mantz H, Jacobs K, Mecke K. Utilizing Minkowski functionals for image analysis: A marching square algorithm. *J Stat Mech: Theory Exper*. 2008;2008:1-29.

37. Klenk S, Schmidt V, Spodarev E. A new algorithmic approach to the computation of Minkowski functionals of polyconvex sets. *Comput Geom*. 2006;34:127-148.

38. Guderlei R, Klenk S, Mayer J, Schmidt V, Spodarev E. Algorithms for the computation of the Minkowski functionals of deterministic and random polyconvex sets. *Image Vision Comput*. 2007;25:464-474.

39. Alesker S. Description of Continuous Isometry Covariant Valuations on Convex Sets. *Geometriae Dedicata*. 1999;74:241-248.

40. Hug D, Schneider R, Schuster R. The space of isometry covariant tensor valuations. *St Petersburg Math J*. 2008;19:137-158.

41. Hug D, Schneider R, Schuster R. Integral geometry of tensor valuations. *Adv Appl Math*. 2008;41:482-509.

42. Jensen EBV, Kiderlen M, eds. *Tensor Valuations and Their Applications in Stochastic Geometry and Imaging*, Lecture Notes in Mathematics, vol. 2177. Cham: Springer; 2017.

43. Schröder-Turk GE, Mickel W, Kapfer SC, et al. Minkowski Tensor Shape Analysis of Cellular, Granular and Porous Structures. *Adv Mater*. 2011;23:2535-2553.

44. Klatt M, Schröder-Turk GE, Mecke K. Mean-intercept anisotropy analysis of porous media. II. Conceptual shortcomings of the MIL tensor definition and Minkowski tensors as an alternative. *Med Phys*. 2017;44:3663-3675.

45. Schröder-Turk GE, Mickel W, Kapfer SC, et al. Minkowski tensors of anisotropic spatial structure. *New J Phys*. 2013;15:1-38.

46. Svane AM. Estimation of Intrinsic Volumes from Digital Grey-Scale Images. *J Math Imaging Vision*. 2014;49:352-376.

47. Svane AM. Estimation of Minkowski tensors from digital grey-scale images. *Image Anal Sterol*. 2015;34:51-61.

48. Hug D, Kiderlen M, Svane AM. Voronoi-based estimation of Minkowski tensors from finite point samples. *Discret Comput Geom*. 2017;57:545-570.

49. Zähle M. Integral and current representation of Federer's curvature measures. *Arch Math (Basel)*. 1986;46(6):557-567. doi:10.1007/BF01195026

50. Schneider R. *Convex Bodies: The Brunn-Minkowski theory*. expanded, Encyclopedia of Mathematics and its Applications, vol. 151. Cambridge: Cambridge University Press; 2014.

51. Klenk S, Schmidt V, Spodarev E. A new algorithmic approach to the computation of Minkowski functionals of polyconvex sets. *Comput Geom*. 2006;34(3):127-148. doi:10.1016/j.comgeo.2006.02.002

52. Rataj J. Estimation of intrinsic volumes from parallel neighbourhoods. *Rend Circ Mat Palermo (2) Suppl*. 2006;77:553-563. MR2245722

53. Schneider R. Tensor valuations on convex bodies and integral geometry. *Rendiconti del Circolo Matematico di Palermo Series II*. 2000;65:295-316.

54. Klusemann B, Svendsen B. Homogenization methods for multi-phase elastic composites: Comparisons and benchmarks. *Technische Mechanik*. 2010;4:374-386.

55. Hug D, Schneider R. Hölder continuity for support measures of convex bodies. *Arch Math (Basel)*. 2015;104(1):83-92. doi:10.1007/s00013-014-0719-0

56. Lenoir A. Fast Estimation of Mean Curvature on the Surface of a 3D Discrete Object. *Discret Geom Comput Imagery*. 1997;1347:175-186.

57. Monga O, Ayache N, Sander PT. From voxel to curvature. In: Geometric methods in computer vision, Vol. 1570. SPIE; 1991:382-390.

58. Heinecke F, Willberg C. Manufacturing-Induced Imperfections in Composite Parts Manufactured via Automated Fiber Placement. *J Compos Sci*. 2019;3:1-24.

59. Ambrosio L, Fusco N, Pallara D. *Functions of Bounded Variation and Free Discontinuity Problems*. Oxford: Oxford University Press; 2000.

60. Cooley JW, Turkey JW. An algorithm for the machine calculation of complex Fourier series. *Math Comput*. 1965;19:297-301.

61. Bredies K, Lorenz D. *Mathematical Image Processing*. Cham, Switzerland: Springer; 2018.

62. Olver PJ. *Introduction to Partial Differential Equations*. Cham, Switzerland: Springer; 2014.

63. Giusti E. *Minimal Surfaces and Functions of Bounded Variation* Borel A, Moser J, Yau S-T, eds., Monographs in Mathematics, vol. 80. Boston: Birkhäuser; 1984.

64. Maggi F. *Sets of Finite Perimeter and Geometric Variational Problems: An Introduction to Geometric Measure Theory*: Cambridge University Press; 2012.

65. Behnel S, Bradshaw R, Citro C, Dalcin L, Seljebotn DS, Smith K. Cython: The Best of Both Worlds. *Comput Sci Eng*. 2011;13(2):31-39.

66. Anderson E, Bai Z, Bischof C, et al. *LAPACK Users' Guide*. Third. Philadelphia: Society for Industrial and Applied Mathematics; 1999.

67. Jones RM. *Mechanics of Composite Materials*. 2nd ed. Boca Raton, USA: Taylor & Francis; 1998.

68. Chung ST, Kwon TH. Numerical Simulation of Fiber Orientation in Injection Molding of Short-Fiber-Reinforced Thermoplastics. *Polymer Eng Sci*. 1995;35:604-618.

69. Bay RS, Tucker III CL. Stereological measurement and error estimates for three dimensional fiber orientation. *Polymer Eng Sci*. 1992;32:240-253.

70. Pinter P, Dietrich S, Bertram B, Kehrer L, Elsner P, Weidenmann KA. Comparison and error estimation of 3D fibre orientation analysis of computed tomography image data for fibre reinforced composites. NDT and E International, 26–35; 2018.

71. Hessman PA, Riedel T, Welschinger F, Hornberger K, Böhlke T. Microstructural analysis of short glass fiber reinforced thermoplastics based on x-ray micro-computed tomography. *Compos Sci Technol*. 2019;183:1-10.
72. Inceoglu F, Ville J, Ghamri N, et al. Correlation Between Processing Conditions and Fiber Breakage During Compounding of Glass Fiber-Reinforced Polyamide. *Polymer Compos*. 2011;32:1842-1850.
73. Schneider M. The Sequential Addition and Migration method to generate representative volume elements for the homogenization of short fiber reinforced plastics. *Comput Mech*. 2017;59:247-263.
74. Tyler DE. Statistical Analysis for the Angular Central Gaussian Distribution on the Sphere. *Biometrika*. 1987;74(3):579-589.
75. Montgomery-Smith S, Jack D, Smith DE. The Fast Exact Closure for Jeffery's equation with diffusion. *J Non-Newtonian Fluid Mech*. 2011;166:343-353.
76. Wirjadi O, Schladitz K, Rack A, Breuel T. Applications of anisotropic image filters for computing 2D and 3D-fiber orientations. In: Proceedings of the 10th european congress of iss; 2009:107-112.
77. Rao TV. *Metal Casting: Principles and Practice*. New Delhi, Switzerland: New Age International; 2003.
78. Schneider M, Hofmann T, Andrä H, et al. Modelling the microstructure and computing effective elastic properties of sand core materials. *Int J Solids Struct*. 2018;143:1-17.
79. Mickel W, Kapfer SC, Schröder-Turk GE, Mecke K. Shortcomings of the bond orientational order parameters for the analysis of disordered particulate matter. *J Chem Phys*. 2013;138:44501.
80. Klatt MA, Göring D, Stegmann C, Mecke K. Shape analysis of counts maps. *AIP Confer Proc*. 2012;1505(1):737-740.
81. Göring D, Klatt MA, Stegmann C, Mecke K. Morphometric analysis in gamma-ray astronomy using Minkowski functionals. *Astron Astrophys*. 2013;555(A38):1-7.
82. Benveniste Y. A new approach to the application of Mori-Tanaka's theory in composite materials. *Mech Mater*. 1987;6:147-157.
83. Kehrer L, Wicht D, Wood JT, Böhlke T. Dynamic mechanical analysis of pure and fiber-reinforced thermoset- and thermoplastic-based polymers and free volume-based viscoelastic modeling. *GAMM-Mitteilungen*. 2018;48:1-16.

APPENDIX A: MINKOWSKI TENSORS FOR SPECIFIC SHAPES

A.1 | Minkowski tensor of a ball

Consider the ball $B_R(0)$, parameterized by spherical coordinates (r, φ, θ), with $r \in [0, R]$, $\varphi \in [0, 2\pi]$, and $\theta \in [0, \pi]$. The transformation to Cartesian coordinates reads

$$\mathbf{x}(r, \varphi, \theta) = \begin{pmatrix} r\sin(\theta)\cos(\varphi) \\ r\sin(\theta)\sin(\varphi) \\ r\cos(\theta) \end{pmatrix}.$$

The outward-pointing unit normal on $\partial B_R(0)$ is given by $\mathbf{n}(r, \varphi, \theta) = \mathbf{x}(1, \varphi, \theta)$ and is thus independent of r. With this parameterization at hand, the Minkowski tensor $W_1^{0,2}$ computes as follows:

$$
\begin{aligned}
W_1^{0,2}(B_R(0)) &= \frac{R^2}{3} \int_0^{2\pi} \int_0^\pi \mathbf{n}(\varphi, \theta) \otimes \mathbf{n}(\varphi, \theta) \sin(\theta) \mathrm{d}\theta \mathrm{d}\varphi \\
&= \frac{R^2}{3} \int_0^{2\pi} \int_0^\pi \begin{pmatrix} \sin^2(\theta)\cos^2(\varphi) & \sin^2(\theta)\sin(\varphi)\cos(\varphi) & \sin(\theta)\cos(\theta)\cos(\varphi) \\ \sin^2(\theta)\sin(\varphi)\cos(\varphi) & \sin^2(\theta)\sin^2(\varphi) & \sin(\theta)\cos(\theta)\sin(\varphi) \\ \sin(\theta)\cos(\theta)\cos(\varphi) & \sin(\theta)\cos(\theta)\sin(\varphi) & \cos^2(\theta) \end{pmatrix} \sin(\theta)\mathrm{d}\theta\mathrm{d}\varphi \\
&= \frac{4\pi R^2}{9}\mathrm{Id}.
\end{aligned}
$$

A.2 | Minkowski tensor of a cylinder

We consider a cylinder K in $\mathbb{R}^3$, oriented in z-direction. We parameterize it by cylindrical coordinates (r, φ, z) with $r \in [0, R)$, $\varphi \in [0, 2\pi]$ and $z \in (0, L)$. The transformation to Cartesian coordinates reads

$$\mathbf{x}(r, \varphi, z) = \begin{pmatrix} r\cos(\varphi) \\ r\sin(\varphi) \\ z \end{pmatrix}.$$

We divide the boundary into three subsets, describing the side, top, and bottom of the cylinder $\partial K = \partial K_s \cup \partial K_t \cup \partial K_b$. The side ∂K_s is parameterized by $r = R$, $\varphi \in (0, 2\pi]$, $z \in [0, L]$; the bottom ∂K_b by $r \in [0, R]$, $\varphi \in (0, 2\pi]$, $z = 0$; and the top ∂K_t by $r \in [0, R]$, $\varphi \in (0, 2\pi]$, $z = L$. The outward-pointing unit normals for the side, bottom, and top boundary, respectively, read

$$\mathbf{n}_s = \begin{pmatrix} \cos(\varphi) \\ \sin(\varphi) \\ 0 \end{pmatrix}, \ \mathbf{n}_t = \begin{pmatrix} 0 \\ 0 \\ 1 \end{pmatrix} \text{ and } \mathbf{n}_b = \begin{pmatrix} 0 \\ 0 \\ -1 \end{pmatrix}.$$

With this parametrization at hand, we compute the Minkowski tensor $W_1^{0,2}$ of K by

$$
\begin{aligned}
W_1^{0,2}(K) &= \frac{1}{3}\int_0^{2\pi}\int_0^L \begin{pmatrix} \cos^2(\varphi) & \cos(\varphi)\sin(\varphi) & 0 \\ \cos(\varphi)\sin(\varphi) & \sin^2(\varphi) & 0 \\ 0 & 0 & 0 \end{pmatrix} R\,\mathrm{d}\varphi\mathrm{d}z + \frac{2}{3}\int_0^R\int_0^{2\pi} \mathbf{e}_z \otimes \mathbf{e}_z r\,\mathrm{d}r\mathrm{d}\varphi \\
&= \frac{\pi}{3}LR(\mathbf{e}_x \otimes \mathbf{e}_x + \mathbf{e}_y \otimes \mathbf{e}_y) + \frac{2\pi}{3}R^2 \mathbf{e}_z \otimes \mathbf{e}_z \\
&= \frac{2\pi}{3}R^2 \left[\mathbf{e}_z \otimes \mathbf{e}_z + \frac{L}{2R}(\mathrm{Id} - \mathbf{e}_z \otimes \mathbf{e}_z) \right].
\end{aligned}
$$

Dividing $W_1^{0,2}(K)$ by its trace gives the QNT of K:

$$\mathrm{QNT}(K) = \frac{R}{R+L}\mathbf{e}_z \otimes \mathbf{e}_z + \frac{L}{2(R+L)}(\mathrm{Id} - \mathbf{e}_z \otimes \mathbf{e}_z).$$

If $R \ll L$ holds, then $R/(R + L)$ is the smallest eigenvalue, which indicates an extension in $\mathbf{e}_z$-direction. The larger eigenvalue $L/(2(R + L))$ has multiplicity 2, indicating some symmetry within the $\mathbf{e}_x - \mathbf{e}_y$-plane.

If $R \gg L$ holds, the smaller eigenvalue has multiplicity 2, indicating a disc-like shape within the $\mathbf{e}_x - \mathbf{e}_y$-plane.